nature medicine

Pericyte degeneration causes white matter dysfunction in the mouse central nervous system

Axel Montagne[1,2,9], Angeliki M Nikolakopoulou[1,2,9], Zhen Zhao[1,2,9], Abhay P Sagare[1,2], Gabriel Si[1], Divna Lazic[1–3], Samuel R Barnes[4], Madelaine Daianu[5], Anita Ramanathan[1,2], Ariel Go[1], Erica J Lawson[1,2], Yaoming Wang[1,2], William J Mack[6], Paul M Thompson[5], Julie A Schneider[7], Jobin Varkey[1,2], Ralf Langen[1,2], Eric Mullins[8], Russell E Jacobs[1,2,4] & Berislav V Zlokovic[1,2]

Diffuse white-matter disease associated with small-vessel disease and dementia is prevalent in the elderly. The biological mechanisms, however, remain elusive. Using pericyte-deficient mice, magnetic resonance imaging, viral-based tract-tracing, and behavior and tissue analysis, we found that pericyte degeneration disrupted white-matter microcirculation, resulting in an accumulation of toxic blood-derived fibrin(ogen) deposits and blood-flow reductions, which triggered a loss of myelin, axons and oligodendrocytes. This disrupted brain circuits, leading to white-matter functional deficits before neuronal loss occurs. Fibrinogen and fibrin fibrils initiated autophagy-dependent cell death in oligodendrocyte and pericyte cultures, whereas pharmacological and genetic manipulations of systemic fibrinogen levels in pericyte-deficient, but not control mice, influenced the degree of white-matter fibrin(ogen) deposition, pericyte degeneration, vascular pathology and white-matter changes. Thus, our data indicate that pericytes control white-matter structure and function, which has implications for the pathogenesis and treatment of human white-matter disease associated with small-vessel disease.

© 2018 Nature America, Inc., part of Springer Nature. All rights reserved.

White matter is composed of myelinated axon tracts that maintain connections between individual neurons in different gray-matter regions. Diffuse white-matter disease is prevalent in the elderly and is associated with small-vessel disease[1], which contributes to approximately 50% of all dementias worldwide, including Alzheimer's disease (AD)[2–4]. Individuals with AD develop early white-matter changes[5,6], with loss of oligodendrocytes and axons[7] being concomitant with cerebral vessel pathology, loss of vascular integrity and blood-flow reductions[8–11]. Despite the prevalence and clinical importance of age-related white-matter disease associated with small-vessel disease, the underlying biological mechanisms remain elusive.

We investigated whether brain capillary pericytes, embedded in the wall of smallest brain vessels[12–14], are involved in white-matter health and disease. Pericytes control microvascular functions in neuron-dense gray-matter regions, including blood-brain barrier (BBB) permeability[15–17] and cerebral blood flow[18–22]. They die in AD[10,23–26], mild dementia[27], stroke[19,20] and cerebral autosomal dominant arteriopathy with subcortical infarcts (CADASIL), the most common genetic ischemic small-vessel disease associated with cognitive impairment[28]. Nonetheless, the role of pericytes in the pathogenesis of these disorders, particularly the white-matter lesions, remains poorly understood. It is also unclear whether pericytes can control vascular integrity and blood flow in white-matter axon tracts, which lack neuronal cell bodies.

To address these questions, we studied microcirculatory changes in relation to white-matter integrity in pericyte-deficient mice carrying seven point mutations in platelet-derived growth factor receptor β (PDGFRβ), which disrupt PDGFRβ signaling in vascular mural cells, resulting in pericyte loss[29]. Adult *Pdgfrb*$^{F7/F7}$ mice are viable[15,17], but develop early pericyte loss, causing BBB breakdown and microvascular reductions[15,17,29], without appreciable early involvement of vascular smooth muscle cells (VSMCs)[30], making them a valuable model to study the effects of pericyte loss on neurovascular and brain functions.

RESULTS

Loss of white-matter pericyte coverage and capillary integrity in AD

Consistent with previous reports examining gray-matter brain regions in post-mortem AD tissue[23–26], we observed a 50% loss of pericyte coverage and a threefold greater accumulation of blood-derived

[1]Zilkha Neurogenetic Institute, Keck School of Medicine, University of Southern California, Los Angeles, California, USA. [2]Department of Physiology and Neuroscience, Keck School of Medicine, University of Southern California, Los Angeles, California, USA. [3]Department of Neurobiology, Institute for Biological Research, University of Belgrade, Belgrade, Republic of Serbia. [4]Biological Imaging Center, Beckman Institute, California Institute of Technology, Pasadena, California, USA. [5]Imaging Genetics Center, Mark & Mary Stevens Neuroimaging & Informatics Institute, University of Southern California, Marina del Rey, California, USA. [6]Department of Neurological Surgery, Keck School of Medicine, University of Southern California, Los Angeles, California, USA. [7]Alzheimer's Disease Center, Rush University Medical Center, Chicago, Illinois, USA. [8]Division of Hematology and Cancer and Blood Diseases Institute, Cincinnati Children's Hospital Medical Center, University of Cincinnati College of Medicine, Cincinnati, Ohio, USA. [9]These authors contributed equally to this work. Correspondence should be addressed to B.V.Z. (zlokovic@usc.edu).

Received 2 August 2016; accepted 4 January 2018; published online 5 February 2018; doi:10.1038/nm.4482

extravascular fibrin(ogen) deposits (indicative of capillary leakage and loss of vascular integrity) in the subcortical white matter of AD patients compared with controls (**Fig. 1a–c** and **Supplementary Table 1**). This has been shown by immunostaining for pericyte marker PDGFRβ[14,17], fluorescent staining of endothelial-specific marker lectin[17] and immunostaining of fibrin(ogen), with quantification analysis of pericyte coverage and fibrin(ogen) extravascular deposits. The microvascular pathology in AD white matter was associated with 50% loss of oligodendrocytes, as shown by immunostaining for oligodendrocyte lineage transcription factor 2 (Olig2)[31], as well as loss of myelin, as indicated by immunostaining for myelin basic protein (MBP)[31] (**Supplementary Fig. 1**), consistent with previous findings in the white matter in AD[7].

Blood-axon barrier and blood-flow disruptions in the white matter of pericyte-deficient mice

To assess whether pericyte loss causes white-matter vascular pathology and degeneration, we employed the pericyte-deficient *Pdgfrb*$^{F7/F7}$ (F7/F7) mouse model[16,17,30,32]. Using a dynamic contrast-enhanced magnetic resonance imaging (MRI) protocol with post-processing Patlak analysis[27], we quantified regional white-matter tract vascular permeability to intravenously injected gadolinium-based contrast agent. In white-matter tracts, including corpus callosum (**Fig. 1d**,**e**), internal capsule, cingulum and external capsule (**Supplementary Fig. 2a–d**), we found a progressive increase in the capillary permeability transfer constant (K_{trans}) in 4–6-, 12–16- and 36–48-week-old F7/F7 mice compared with age-matched *Pdgfrβ*$^{+/+}$ littermate controls. We also observed a progressive loss of white-matter capillary pericyte coverage in the corpus callosum (**Fig. 1f**,**g**) and other white matter tracts (**Supplementary Fig. 3c**,**d**) of 2-, 4–6-, 12–16- and 36–48-week-old F7/F7 mice, along with a loss of total pericyte numbers (**Supplementary Fig. 3a**,**b**). Blood-derived fibrin(ogen) extravascular deposits progressively accumulated in the corpus callosum and other white matter tracts of 4–6-, 12–16- and 36–48-week-old F7/F7 mice (**Fig. 1f**,**h**,**i** and **Supplementary Fig. 4a**,**b**). White-matter fibrin(ogen) deposits were not detectable; however, in 2-week-old F7/F7 mice (**Fig. 1h** and **Supplementary Fig. 4a**,**b**), despite the presence of circulating exogenous tracer Alexa Fluor 555-cadaverin in white matter (**Fig. 1i**) and its cellular uptake by oligodendrocytes, pericytes and microglia (**Supplementary Fig. 4c**,**d**), indicative of disrupted white-matter vascular integrity.

In contrast, cadaverine uptake in littermate controls was undetectable, suggesting that pericyte loss and blood-axon barrier breakdown precede white-matter accumulation of fibrin(ogen) in F7/F7 mice. Beginning at 4–6 weeks of age, the degree of fibrinogen deposits correlated with the loss of pericyte coverage (**Fig. 1j** and **Supplementary Fig. 4e**,**f**). Compared with gray-matter regions (for example, cortex, hippocampus), the white-matter tracts of young 12–16-week-old F7/F7 mice accumulated substantially higher levels of blood-derived fibrin(ogen) (**Fig. 1k**) and hemosiderin deposits (**Fig. 1l**,**m**).

Using a modified dynamic susceptibility-contrast (DSC)-MRI technique originally developed for cerebral blood-flow measurements in humans (Online Methods), we quantified local blood flow in white-matter tracts in mice. The blood-flow maps and quantification revealed progressive blood-flow reductions in the corpus callosum (**Fig. 1n**,**o**), internal capsule, cingulum and external capsule (**Supplementary Fig. 5a–d**) of F7/F7 mice compared with controls. The white-matter tracts in F7/F7 mice developed greater absolute blood-flow reductions than the gray-matter regions (**Supplementary Fig. 5e–h**). Notably, we did not find changes in the white-matter blood flow in 2-week-old F7/F7 mice (**Supplementary Fig. 5i**), suggesting that pericyte loss and disruption of vascular integrity in the present model precede blood-flow changes. Quantitative ^{14}C-iodoantipyrine autoradiography, a 'gold-standard' for regional cerebral blood flow analysis in mice[17,33], corroborated DSC-MRI findings showing comparable blood-flow reductions in the white-matter tracts of F7/F7 mice (**Supplementary Fig. 6a–d**). Vascular density in the white-matter regions of control mice was approximately 2–3-fold lower than in the gray-matter regions (**Supplementary Fig. 7a**,**b**), which is consistent with lower blood-flow values. The capillary density in white matter was further reduced in F7/F7 mice compared with controls, as shown in 12–16-week-old animals (**Supplementary Fig. 7a**,**b**). Loss of white-matter microvascular density positively correlated with the loss of pericyte coverage (**Supplementary Fig. 7c**), similar to that reported for gray-matter regions in pericyte-deficient mice[17,30]. Moreover, white-matter blood-flow reductions correlated positively with losses of pericyte coverage and microvascular density, as illustrated in the corpus callosum (**Supplementary Fig. 7d**,**e**).

White-matter structural changes and loss of connectivity in pericyte-deficient mice

High-resolution diffusion tensor imaging (DTI)-MRI (**Supplementary Fig. 8a**) did not reveal changes in the white matter, cortical or hippocampal volumes in 4–6-week-old F7/F7 mice compared with controls (**Fig. 2a–c**). However, at 12–16 weeks of age, F7/F7 mice developed white-matter atrophy, which worsened by age (**Fig. 2a**). In contrast, no detectable changes were found in the cortex (**Fig. 2b**) or hippocampus (**Fig. 2c**) volumes in 12–16-week-old F7/F7 mice. A moderate loss of gray-matter volume was found in 36–48-week-old F7/F7 mice compared with their age-matched controls (**Fig. 2b**,**c**). Consistent with these findings, post-processing DTI analysis showed no detectable changes in the white-matter structure in 4–6-week-old F7/F7 mice, as indicated by normal fractional anisotropy (**Fig. 2d** and **Supplementary Fig. 8b**) and mean, radial and axial diffusivity values (**Supplementary Fig. 8b**,**c**). However, 12–16-week-old F7/F7 mice showed white-matter disorganization and damage, as demonstrated in several regions displaying decreased fractional anisotropy (**Fig. 2e** and **Supplementary Fig. 8d**) and changes in radial, axial and mean diffusivity values (**Supplementary Fig. 8d**,**e**), respectively. These changes worsened with age, as shown in 36–48-week-old F7/F7 mice (**Fig. 2f** and **Supplementary Fig. 8f**,**g**). Using high-resolution DTI-based tractography[34] (**Fig. 2g**), we found 30–40% fiber loss and detected shorter, unorganized fibers throughout the white-matter tracts, as illustrated in the corpus callosum and cingulum in 12–16-week-old F7/F7 mice (**Fig. 2g–i**). These changes worsened with age, as shown in 36–48-week-old F7/F7 mice (**Fig. 2g–i**). No detectable changes were found in younger 4–6-week-old F7/F7 mice (**Fig. 2g–i**).

Next, we performed anterograde tract-tracing with a fluorescent adeno-associated virus expressing GFP (AAV-eGFP)[35]. The AAV-eGFP construct was injected stereotaxically into the primary somatosensory barrel cortex (**Fig. 2j**). After 21 d, 12–16-week-old F7/F7 mice showed reductions in the integrated projection density toward the contralateral somatosensory barrel primary cortex, throughout the corpus callosum and toward the internal capsule (**Fig. 2j**,**k** and **Supplementary Fig. 9a–d**). Quantification of viral-based tract-tracing data corroborated DTI-tractography results, revealing a 30–40% decrease in the fiber density in the studied white-matter tracts in 12–16-week-old F7/F7 mice and a greater loss of projections by 45–70% in 36–48-week-old F7/F7 mice (**Fig. 2k** and **Supplementary Fig. 9a–d**).

© 2018 Nature America, Inc., part of Springer Nature. All rights reserved.

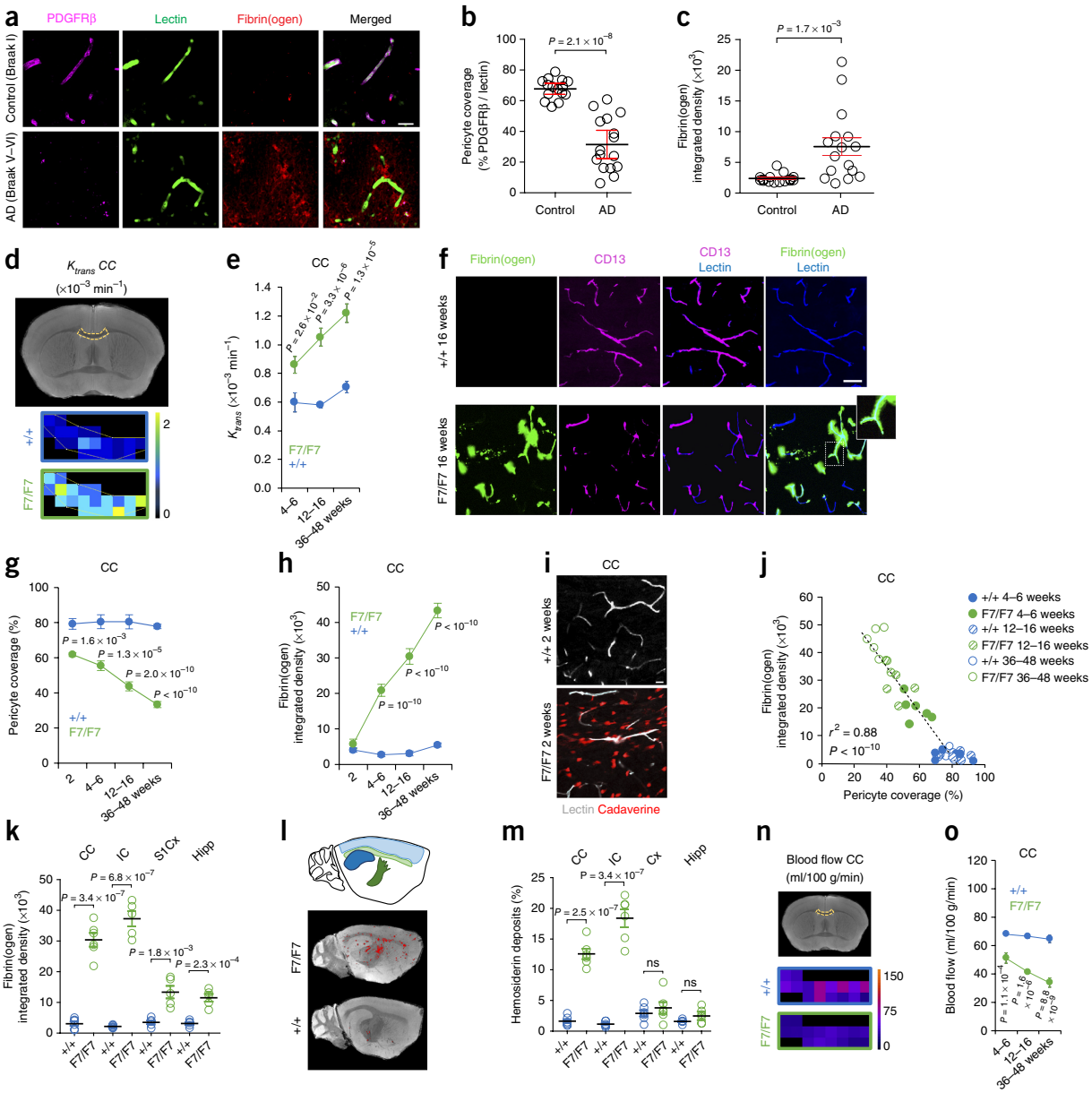

Figure 1 White-matter microvascular changes in AD and pericyte-deficient mice. (**a**) PDGFRβ-positive pericyte coverage (magenta), lectin-positive endothelial profiles (green) and extravascular fibrin(ogen) deposits (red) in the prefrontal subcortical white matter of an age-matched control (Braak I, upper) and AD case (Braak V–VI, lower). Scale bar represents 20 μm. (**b**,**c**) Quantification of pericyte coverage (**b**) and fibrin(ogen)-positive extravascular deposits (**c**) in the prefrontal subcortical white matter of controls ($n = 15$) and AD cases ($n = 16$). Data are presented as mean ± s.e.m. See **Supplementary Table 1** for clinical and neuropathological characteristics. (**d**) Representative K_{trans} maps in the corpus callosum (CC) of 16-week-old F7/F7 and age-matched littermate control (*+/+*) mice generated from DCE-MRI scans. (**e**) The regional K_{trans} CC values in 4–6-, 12–16- and 36–48-week-old F7/F7 (green) and age-matched littermate control (*+/+*; blue) mice. Data are presented as mean ± s.e.m.; $n = 6$ 4–6-week-old mice per group; $n = 7$ 12–16-week-old mice per group; $n = 5$ 36–48-week-old mice per group. (**f**) Fibrin(ogen)-positive extravascular deposits (green), CD13-positive pericyte coverage (magenta) and lectin-positive endothelial profiles (blue) in the CC of 16-week-old F7/F7 and control (*+/+*) mice. Scale bar represents 40 μm. (**g**,**h**) Quantification of pericyte coverage in the CC of 2-, 4–6-, 12–16- and 36–48-week-old F7/F7 (green) and control (*+/+*, blue) mice (**g**), and quantification of fibrin(ogen) deposits in the CC of 2-, 4–6-, 12–16- and 36–48-week-old F7/F7 (green) and control (*+/+*, blue) mice (**h**). Data are presented as mean ± s.e.m.; $n = 6$ mice per group. (**i**) Representative images of five independent replicates of the CC showing lectin-positive endothelial profiles (white) and cellular uptake of Alexa Fluor 555-conjugated cadaverine (red) in 2-week-old F7/F7 and control (+/+) mice. Scale bar represents 20 μm. (**j**) Negative correlation between fibrin(ogen) extravascular deposits and pericyte coverage in the CC; $n = 36$ individual points from F7/F7 and control (*+/+*) mice at different age; r^2, Pearson's coefficient. (**k**) Fibrin(ogen) deposits in the CC and internal capsule (IC), and the primary somatosensory barrel cortex (S1Cx) and dorsal hippocampus (Hipp) of the gray matter in 12–16-week-old F7/F7 and control (+/+) mice. Data are presented as mean ± s.e.m.; $n = 6$ mice per group for CC and $n = 5$ mice per group for IC, S1Cx and Hipp. (**l**,**m**) High-resolution T2*-weighted images (sagittal plane) of iron-containing hemosiderin deposits (red dots) in 16-week-old F7/F7 (upper) and control (+/+, lower) mice (**l**), and quantification of hemosiderin deposits in the white matter (CC and IC) and gray matter (Cx and Hipp) regions in 12–16-week-old F7/F7 mice and control (+/+) mice (**m**). Data are presented as mean ± s.e.m.; $n = 6$ mice per group. (**n**) The blood flow maps in the CC in 16-week-old F7/F7 and littermate control (*+/+*) mice generated from dynamic contrast-susceptibility MRI scans. (**o**) The regional blood flow values in CC in 4–6-, 12–16- and 36–48-week-old F7/F7 (green) and littermate control (*+/+*, blue) mice. Data are presented as mean ± s.e.m.; $n = 6$ 4–6-week-old mice per group; $n = 7$ 12–16-week-old mice per group; $n = 5$ 36–48-week-old mice per group. In **e**, **g**, **h** and **o**, one-way ANOVA and Bonferroni's *post* hoc tests were used. Unpaired two-tailed Student's *t* tests were used for **b**, **c**, **k** and **m**; ns = non-significant ($P > 0.05$).

© 2018 Nature America, Inc., part of Springer Nature. All rights reserved.

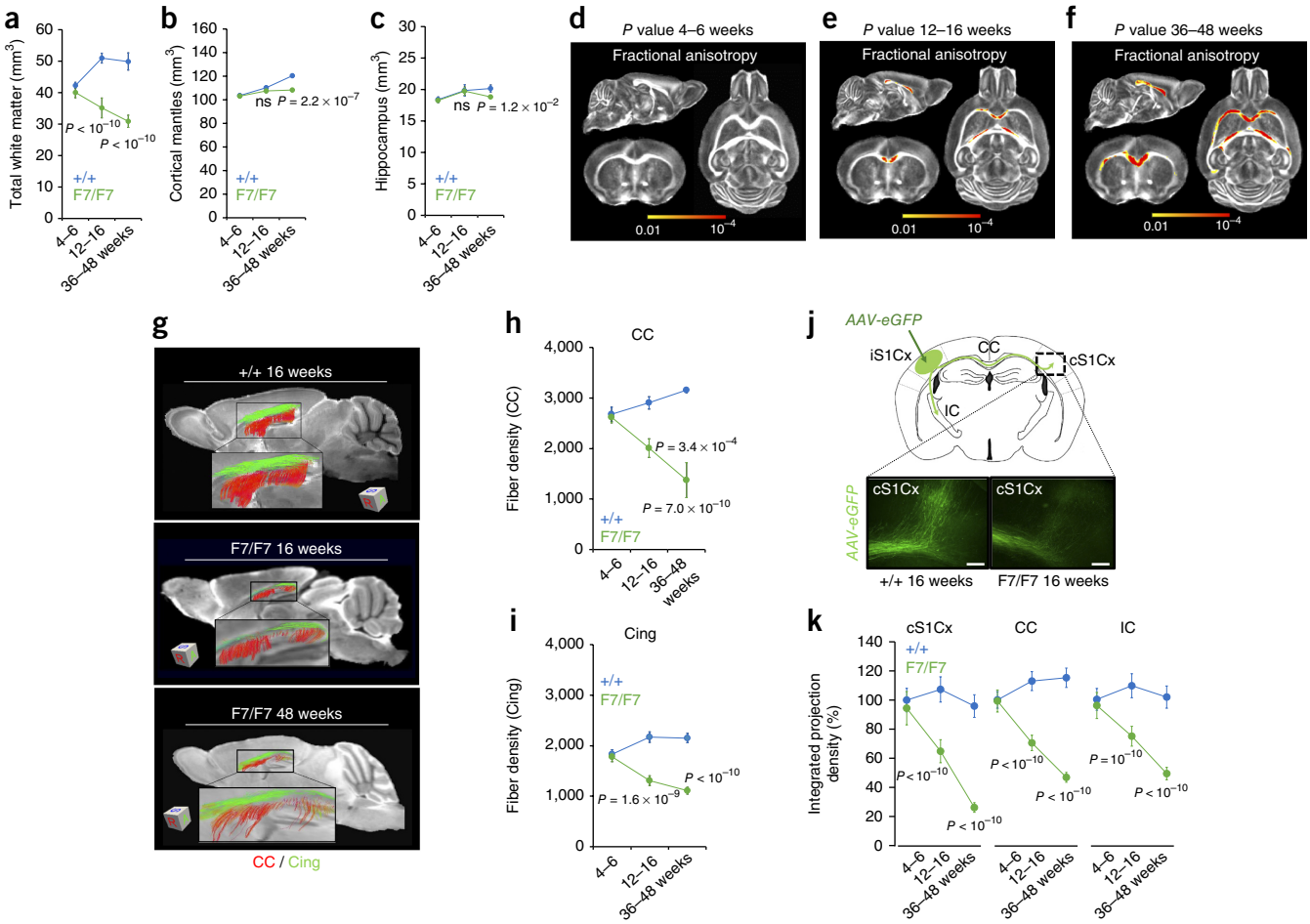

Figure 2 White-matter structural changes and loss of connectivity in pericyte-deficient mice. (**a**–**c**) Total white-matter (**a**), cortical mantles (**b**) and hippocampus (**c**) volumes in 4–6-, 12–16-, and 36–48-week-old F7/F7 (green) and age-matched littermate control (+/+, blue) mice. Data are presented as mean ± s.d.; $n = 6$ 4–6-week-old mice per group; $n = 7$ 12–16-week-old mice per group; $n = 7$ 36–48-week-old mice per group. (**d**–**f**) Probabilistic *P* value maps for fractional anisotropy generated from DTI-MRI scans in 4–6- (**d**), 12–16- (**e**) and 36–48-week-old (**f**) F7/F7 and control (+/+) mice. Yellow-red voxels, statistically significant changes in the white matter tracts in 12–16-week-old (**e**) and 36–48-week-old (**f**) F7/F7 mice compared with their age-matched littermate controls (*+/+*) by searchlight-based multivoxel pattern analysis (Online Methods). No changes were found in younger 4–6-week-old (**d**) F7/F7 mice. *P* value color scale from 0.01 to 10^{-4}; $n = 6$ 4–6-week-old mice per group; $n = 7$ 12–16-week-old mice per group; $n = 7$ 36–48-week-old mice per group. (**g**) Fiber tract maps of the corpus callosum (CC, red) and cingulum (Cing, green) generated from DTI-MRI scans in 16-week-old control (+/+, top), 16-week-old F7/F7 (middle), and 48–week-old F7/F7 (bottom) mice. (**h**,**i**) Fiber density quantification in the CC (**h**) and Cing (**i**) from reconstructed tract maps. Data are presented as mean ± s.e.m.; $n = 5$ mice per group. (**j**) A diagram showing the injection site in the ipsilateral primary somatosensory barrel cortex (iS1Cx) of adeno-associated virus expressing green fluorescent protein (AAV-eGFP) used for the anterograde tract-tracing, and the studied labeled fiber projections from the iS1Cx to the contralateral S1Cx cortex (cS1Cx), through the CC, and toward the internal capsule (IC). Lower panels denote 3D-labeled projections toward the contralateral cS1Cx 21 d after injection of AAV-eGFP neuron labeling in the ipsilateral iS1Cx of 16-week-old F7/F7 and control (+/+) mice. Scale bar represents 100 μm. (**k**) Quantification of integrated projection density of indicated brain regions in 4–6-, 12–16-, and 36–48-week-old F7/F7 (green) and control (+/+, blue) mice. Data are presented as mean ± s.d.; $n = 5$ mice per group. In **a**–**c**, **h**, **i** and **k**, one-way ANOVA and Bonferroni's *post hoc* tests were used; ns = non-significant ($P > 0.05$).

© 2018 Nature America, Inc., part of Springer Nature. All rights reserved.

White-matter-related functional deficits in pericyte-deficient mice

Behavior testing revealed white-matter-related functional deficits (Online Methods) that were first observed in 12–16-week-old F7/F7 mice, consistent with reported white-matter structural changes (**Fig. 2**). These animals exhibited reduced maximum velocity on the complex running wheel test (**Fig. 3a**) and a specific impairment in spatial working memory on eight-arm radial maze test showing an increase in revisiting errors (**Fig. 3b**,**c**). In contrast, younger 4–6-week-old F7/F7 mice performed similarly to controls on both tests (**Fig. 3a**,**c**), as expected by the lack of white-matter structural changes observed by MRI and connectomics analysis at this early stage (**Fig. 2**). White-matter-related deficits worsened with age, as shown by a substantial decrease in velocity on the complex running wheel test in 36–48-week-old F7/F7 mice compared with age-matched controls (**Fig. 3a**). Tests involving hippocampus-dependent behavior, such as novel object recognition and fear conditioning, and daily activity tests, such as nesting and burrowing (**Fig. 3d**–**g**), revealed no differences between 4–6- and 12–16-week-old F7/F7 mice compared with their respective age-matched controls, consistent with undetectable changes in the hippocampus volume (**Fig. 2c**) and normal neuron numbers (see below). However, using these tests, we found deficits in F7/F7 mice at 36–48 weeks of age (**Fig. 3d**,**f**,**g**), consistent with much greater (40%) white-matter total loss (**Fig. 2a**) and a substantial loss of the white matter fibers (**Fig. 2g**–**i**,**k**) associated with a moderate hippocampal and cortical atrophy (**Fig. 2b**,**c**) and detectable neuronal loss (see below).

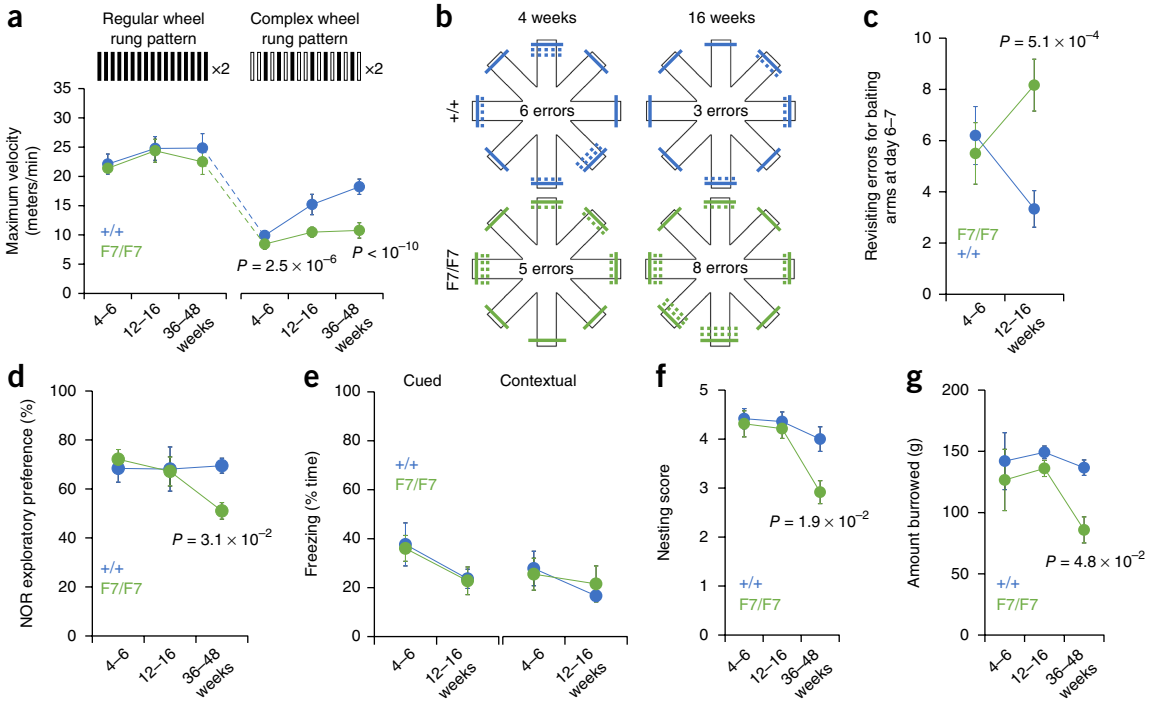

Figure 3 White-matter-related functional deficits in pericyte-deficient mice. (**a**) Maximum velocity on regular and complex running wheel in 4–6-, 12–16-, and 36–48-week-old F7/F7 (green) and control (+/+, blue) mice. Data are presented as mean ± s.e.m.; $n = 8$ mice per group. (**b**,**c**) Diagram showing the number of revisiting errors for baiting on radial eight-arm maze test in 4- and 16-week-old F7/F7 (green) and control (+/+, blue) mice (**b**; solid lines, first entries; dotted lines, revisiting errors), and quantification (**c**) in 4–6- and 12–16-week-old F7/F7 (green) and control (+/+, blue) mice. Data are presented as mean ± s.e.m.; $n = 8$ mice per group. (**d**) Novel object recognition (NOR) in 4–6-, 12–16-, and 36–48-week-old F7/F7 (green) and *+/+* control (blue) mice. Data are presented as mean ± s.e.m.; $n = 8$ 4–6-week-old mice per group; $n = 11$ 12–16-week-old mice per group; $n = 8$ 36–48-week-old mice per group. (**e**) Cued and contextual fear conditioning tests in 4–6 and 12-16-week-old F7/F7 (green) and *+/+* control (blue) mice. Data are presented as mean ± s.e.m.; $n = 8$ 4–6-week-old mice per group; $n = 11$ (cued) and 8 (contextual) 12–16-week-old mice per group. (**f**,**g**) Nesting (**f**) and burrowing (**g**) tests in 4–6-, 12–16-, and 36–48-week-old F7/F7 (green) and *+/+* control (blue) mice. Data are presented as mean ± s.e.m.; $n = 8$ 4–6-week-old mice per group; $n = 11$ 12–16-week-old mice per group; $n = 8$ 36–48-week-old mice per group. In **a** and **c**–**g**, one-way ANOVA and Bonferroni's *post hoc* tests were used.

© 2018 Nature America, Inc., part of Springer Nature. All rights reserved.

Loss of myelin and axons in pericyte-deficient mice

Electron microscopy analysis revealed a loss of myelin and axon degeneration in the corpus callosum of 12–16-week-old F7/F7 mice and a worsening with age compared with age-matched controls, as demonstrated by increased number of degenerated axons, substantial axon loss and an increase in g-ratio indicating thinner myelin sheaths (Online Methods and **Fig. 4a–d**). Similar changes were found in other white-matter regions (**Supplementary Fig. 10a–d**). Immunostaining for MBP and axon neurofilament marker SMI-312 confirmed a loss of myelin and axons in several white-matter regions in 12–16-week-old F7/F7 mice and a worsening with age (**Fig. 4e–g** and **Supplementary Fig. 10e–g**). Luxol fast blue staining and quantification of white-matter damage by Fazekas scale (Online Methods) confirmed the disarrangement of white-matter tracts and appearance of vacuoles in different white-matter regions of 12–16-week-old F7/F7 mice (**Fig. 4h,i** and **Supplementary Fig. 10h,i**). At this time, F7/F7 mice also displayed a 4–6-fold increase in the number of enlarged perivascular spaces in different white-matter regions (**Fig. 4j,k** and **Supplementary Fig. 10j,k**). These enlarged perivascular spaces have been strongly associated with small-vessel disease and white-matter injuries[1,2,36]. Immunoblotting of the corpus callosum homogenates (**Fig. 4l,m**) confirmed reduced MBP levels in 16-week-old F7/F7 mice. No white-matter changes were found in 4–6-week-old F7/F7 mice (**Fig. 4a–d,f,g,i,k–m**).

Notably, there was no neuron loss in the cortex or hippocampus in 12–16-week-old F7/F7 mice, as shown by hematoxylin staining and counting of NeuN-positive (neuron marker) neurons (**Fig. 4n,o Supplementary Fig. 11a–d**). However, there was an approximately 28 and 27% loss of neurons in the cortex and the CA1 hippocampus subfield, respectively, in 36–48-week-old F7/F7 mice, consistent with previous findings showing neuronal loss in pericyte-deficient mice at a later stage[17].

Loss of oligodendrocytes in pericyte-deficient mice

Triple staining for Olig2 (ref. 31), terminal deoxynucleotidyl transferase dUTP nick end labeling (TUNEL) and MBP (**Fig. 5a**) in the corpus callosum of 12–16-week-old F7/F7 mice compared with controls revealed a greater than sevenfold increase in dying oligodendrocytes and approximately 30% decrease in oligodendrocyte density (**Fig. 5b,c**). Dying oligodendrocytes and oligodendrocyte loss were also found in other white-matter regions of 12–16-week-old F7/F7 mice, which worsened in 36–48-week-old F7/F7 mice (**Fig. 5b,c** and **Supplementary Fig. 12a–c**). No changes were observed in 4–6-week-old F7/F7 mice. Given that oligodendrocytes support axons with myelin sheaths[31,37], the loss of oligodendrocytes in F7/F7 mice was consistent with myelin loss and white-matter damage (**Fig. 4a–g**).

Triple immunostaining for multiple oligodendrocyte markers, including platelet-derived growth factor receptor α (PDGFRα),

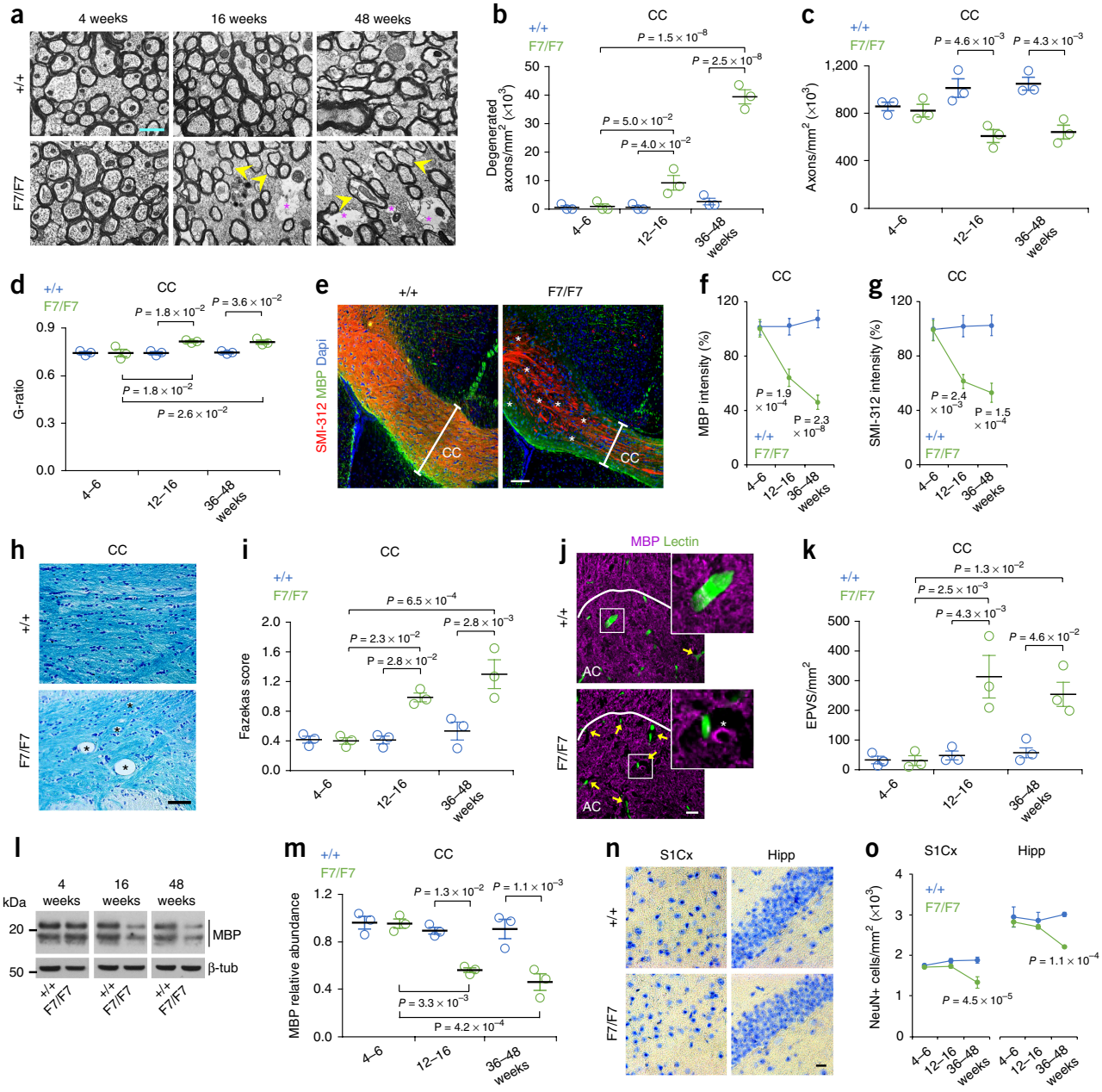

Figure 4 Pericyte-deficient mice develop an early axon degeneration and loss of myelin. (**a**) Electron microscopy analysis of the medial CC in 4-, 16-, and 48-week-old F7/F7 and control (+/+) mice. Yellow arrowheads, thinner myelin sheaths; purple stars, degenerated axons. Scale bar represents 0.5 μm. (**b**–**d**) Quantification of the number of degenerated axons (**b**), total number of axons (**c**) and g-ratio (**d**) in the CC of 4–6-, 12–16- and 36–48-week-old F7/F7 (green) and control (*+/+*, blue) mice. Data are presented as mean ± s.e.m.; $n = 3$ mice per group. (**e**) Immunostaining of myelin basic protein (MBP), neuritic marker SMI-312 and 4',6-diamidino-2-phenylindole (Dapi) nuclear stain in the CC (coronal sections) of 36-week-old F7/F7 and control (+/+) mice. Scale bar represents 100 μm; white bars illustrate CC thickness; stars show MBP and SMI-312 loss. (**f**,**g**) Quantification of MBP (**f**) and SMI-312 (**g**) immunoreactivity in 4–6-, 12–16- and 36–48-week-old F7/F7 (green) and *+/+* (blue) mice. Data are presented as mean ± s.e.m.; $n = 5$ mice per group. (**h**) Luxol fast blue and cresyl violet staining in the CC of 36-week-old F7/F7 and *+/+* control mice. Scale bar represents 100 μm; stars, vacuoles. Representative of three independent replicates. (**i**) Fazekas score for white-matter damage in the CC of in 4–6-, 12–16- and 36–48-week-old F7/F7 (green) and control (+/+, blue) mice. Data are presented as mean ± s.e.m.; $n = 3$ mice per group. (**j**) Immunostaining for MBP and endothelial lectin in the anterior cingulum (AC) tract of 16-week-old F7/F7 and control (*+/+*) mice. Scale bar represents 20 μm; yellow arrows, enlarged perivascular spaces (EPVS). Insets, high magnification of boxed regions; white star, EPVS. (**k**) Quantification of EPVS per mm^2 CC tissue in 4–6-, 12–16- and 36–48-week-old F7/F7 (green) and control (+/+, blue) mice. Data are presented as mean ± s.e.m.; $n = 3$ mice per group. (**l**) MBP immunoblotting of white matter homogenates (pooled corpus callosum, internal capsule, external capsule, cingulum) from 4–6, 12–16, and 36–48-week-old F7/F7 and *+/+* mice. β-tub, β-tubulin loading control. (**m**) MBP relative abundance in 4–6-, 12–16- and 36–48-week-old F7/F7 (green) and control (+/+, blue) mice. Data are presented as mean ± s.e.m.; $n = 3$ mice per group. (**n**) Bright field microscopy (hematoxylin staining) of the primary somatosensory barrel cortex (S1Cx) and CA1 hippocampus subfield (Hipp) in 16-week-old F7/F7 and control (*+/+*) mice. Scale bar represents 50 μm. Representative of three independent replicates. (**o**) Quantification of NeuN-positive neurons in the S1Cx region (layers IV–V) and CA1 hippocampus subfield in 4–6-, 12–16- and 36–48-week-old F7/F7 (green) and control (+/+, blue) mice. Data are presented as mean ± s.e.m.; $n = 5$ mice per group. In **b**–**d**, **f**, **g**, **i**, **k**, **m** and **o**, one-way ANOVA and Bonferroni's *post hoc* tests were used. See **Supplementary Figure 17** for full scans of all western blots for MBP shown in **l**.

© 2018 Nature America, Inc., part of Springer Nature. All rights reserved.

Olig2 and cyclic nucleotide phosphodiesterase (CNPase) in the corpus callosum (**Fig. 5d**), revealed that the number of Olig2 and PDGFRα double-positive oligodendrocyte progenitor cells (OPCs)[31] did not change in 4–6- or 12–16-week-old F7/F7 mice, whereas the number of Olig2 and CNPase double-positive mature oligodendrocytes[31] was substantially decreased in 12–16-week-old F7/F7 mice compared with age-matched littermate controls, which worsened with age (**Fig. 5e**,**f**). Similar results were found in other white-matter regions (**Supplementary Fig. 12d**–**f**). Loss of mature white-matter oligodendrocytes in 12–16-week-old F7/F7 mice compared with controls was confirmed by flow cytometry using anti-MBP and anti-proteolipid protein (PLP) antibodies[31], whereas we found no changes at 4–6 weeks of age (**Fig. 5g**,**h** and **Supplementary Fig. 12g**). Given that genetic ablation of adult oligodendrocytes results in a loss of myelin and axon damage[38], these data support the link between the observed loss of oligodendrocytes, loss of myelin and axon degeneration in F7/F7 mice.

Cerebral white matter and myelinated oligodendrocytes are highly vulnerable to hypoxic and ischemic insults[39,40]. Consistent with early and substantial white-matter blood-flow reductions (**Fig. 1n**,**o**), hypoxyprobe-1 (pimonidazole) administration revealed early hypoxic changes in the white matter (**Fig. 5i**,**j**), but not gray-matter regions (**Supplementary Fig. 12h**–**j**) of 12–16-week-old F7/F7 mice compared with controls, suggesting that hypoxia may contribute to oligodendrocyte cell death and loss. Indeed, hypoxia (that is, oxygen and glucose deprivation) rapidly killed cultured mouse oligodendrocytes within 6 h compared with normoxia, as determined by TUNEL staining (**Fig. 5k**,**l**). Consistent with the high susceptibility of pericytes to hypoxic and ischemic injury[18–20], hypoxia also led to cell death of mouse cultured pericytes (not shown).

Fibrinogen toxicity

Fibrin(ogen) accelerates neurovascular damage, BBB breakdown and neuroinflammation in mouse models of AD[41] and contributes to cognitive impairment in mice and humans[42] and neuron degeneration in AD brains[43]. Soluble fibrinogen inhibits axon outgrowth[44] and leads to CNS inflammatory demyelination[45]. Similarly, fibrin inhibits peripheral nerve remyelination[46] and promotes inflammatory demyelination in models of multiple sclerosis[47,48]. Given that fibrin(ogen) accumulation in the white-matter (**Fig. 1f**,**h**,**j**,**k** and **Supplementary Fig. 4a**,**b**,**e**,**f**) correlated with a loss of pericyte coverage (**Fig. 1j** and **Supplementary Fig. 4e**,**f**) and was associated with a loss of mature oligodendrocytes (**Fig. 5a**–**h**), we next examined whether soluble fibrinogen and fibrin fibrils are toxic to mouse oligodendrocyte and pericyte cultures, and whether pharmacological or genetic manipulations of fibrinogen systemic levels influence white-matter fibrinogen deposition, vascular pathology and white-matter integrity in F7/F7 mice.

Soluble fibrinogen (1.5 mg/ml) did not kill oligodendrocytes within 6 or 12 h of treatment *in vitro* (**Fig. 5l**), but did accumulate intracellularly, as demonstrated at 6 h (**Fig. 5m**), which activated autophagy, a cell-degrading process associated with metabolic stress and cell death[49]. Activation of autophagy was obvious within 12 h of fibrinogen treatment, as indicated by the appearance of autophagy markers such as an elevated microtubule-associated protein 1A/1B-light chain 3 (LC3) ratio (LC3 II/LC3 I) and a decrease in p62 levels[50] (**Fig. 5n**–**p**).

Consistent with findings that autophagy often precedes cell death[51], we also found that fibrinogen administration did not lead to cell death of oligodendrocytes (**Fig. 5l**) or activation of caspase 3 (**Fig. 5q**) within 12 h of treatment, but substantially increased caspase 3 activity (**Fig. 5q** and **Supplementary Fig. 13c**) and dose-dependently killed oligodendrocytes by 24 h after treatment (**Fig. 5r** and **Supplementary Fig. 13a**,**b**). MHY1485, a mTOR activator with inhibitory effect on authophagy[52], and tetrahydroacridinamine-derived autophagy inhibitor VII[53] blocked not only the development of the autophagy markers after 12 h of fibrinogen treatment (**Fig. 5n**–**p**), but also inhibited fibrinogen treatment activation of caspase 3 and cell loss by 24 h after treatment (**Fig. 5q**–**r** and **Supplementary Fig. 13c**), suggesting

Figure 5 Loss of mature oligodendrocytes in pericyte-deficient mice and fibrinogen and fibrin toxicity to mouse oligodendrocytes. (**a**) Confocal images of Olig2 (oligodendrocyte marker), MBP and TUNEL staining in the CC of 16-week-old F7/F7 and control (+/+) mice. Arrows, Olig2- and TUNEL-double positive cells. Scale bar represents 20 μm. (**b**,**c**) Quantification of Olig2- and TUNEL-double positive cells (**b**) and Olig2-positive cells (**c**) in the CC of F7/F7 (green) and control (+/+, blue) mice from 4–6, 12–16 and 36–48 weeks of age. Data are presented as mean ± s.e.m.; $n = 3$ mice per group. (**d**) Confocal images of Olig2, platelet-derived growth factor receptor α (PDGFRα) and cyclic nucleotide phosphodiesterase (CNPase) in the CC of 16-week-old F7/F7 and control (*+/+*) mice). Scale bar represents 20 μm. (**e**,**f**) Quantification of Olig2- and PDGFRα -double positive oligodendrocyte progenitor cells (**e**) and Olig2 and CNPase double-positive myelinated mature oligodendrocytes (**f**) in the CC of 4–6-, 12–16- and 36–48-week-old F7/F7 (green) and *+/+* control (blue) mice. Data are presented as mean ± s.e.m.; $n = 3$ mice per group. (**g**,**h**) Representative dot plots of the flow cytometry analysis of MBP-Alexa647-positive and proteolipid protein (PLP)-Alexa488-positive myelinated mature oligodendrocytes (OLs) (isolated from white matter) from three independent experiments in 12–16-week-old F7/F7 and *+/+* mice (**g**), and quantification of MBP- and PLP-double positive myelinated mature OLs (**h**) in 4–6, 12–16- and 36–48-week-old F7/F7 (green) and control (*+/+*, blue) animals. Data are presented as mean ± s.e.m.; $n = 3$ mice per group. (**i**,**j**) Confocal analysis of hypoxyprobe-1 (pimonidazole)-positive hypoxic tissue ($O_2 < 10$ mm Hg) in the CC in 16-week-old F7/F7 and *+/+* mice (**i**), and quantification of hypoxyprobe-1-positive area (**j**) expressed as the percentage of total tissue in the CC of 4–6- and 12–16-week-old F7/F7 (green) and control (*+/+*, blue) mice. Data are presented as mean ± s.e.m.; $n = 3$ mice per group. Scale bar represents 5 μm. (**k**,**l**) Confocal images of MBP- and TUNEL-double positive cultured primary mouse OLs subjected to oxygen and glucose deprivation (OGD) or vehicle for 6 h (**k**), and quantification of MBP and TUNEL double-positive OLs subjected to OGD or vehicle for 6 h, or treated with fibrinogen (1.5 mg/ml) for 6 h (light gray) and 12 h (dark gray) (**l**). Data are presented as mean ± s.e.m. from three independent experiments (each five coverslips averaged per experiment). Scale bar represents 20 μm. (**m**) Representative images of two MBP and fibrinogen double-positive OLs. Orthogonal views show internalization of fibrinogen 6 h after treatment (1.5 mg/ml). Representative of five independent replicates. Scale bar represents 10 μm. (**n**–**p**) Western blots of autophagy markers LC3-I, LC3-II and p62 (**n**) and their quantification (**o**,**p**) in primary mouse OLs cell lysates after treatment with fibrinogen (1.5 mg/ml), fibrin fibrils (0.1 mg/ml; **Supplementary Fig. 13g**) or vehicle for 12 h with or without MHY1485 (2 μM), a mTOR activator which inhibits autophagy. Western blots are representative of three independent experiments. Scanning densitometry of LC3-I, LC3-II and p62 bands, and LC3-II/LC3-I ratio (**o**) and p62 relative abundance (**p**) normalized with β-actin. For **o** and **p**, mean ± s.e.m. are from three independent experiments. (**q**) Caspase 3 activity at 12 and 24 h after treatment with vehicle, fibrinogen (1.5 mg/ml) or fibrin fibrils (0.1 mg/ml) with and without autophagy inhibitors MHY1485 (2 μM) or inhibitor VII (100 μM). Data are presented as mean ± s.e.m.; $n = 3$ independent experiments. (**r**) Live cells quantified by live and dead assay 24 h after treatment of mature OLs and astrocytes with vehicle, fibrinogen (1.5 mg/ml) or fibrin fibrils (0.1 mg/ml). OLs were also treated with autophagy inhibitors MHY1485 (2 μM) or inhibitor VII (100 μM). Hirudin (4 U/ml) was added to all cultures except in vehicle-control (gray filled circles). Data are presented as mean ± s.e.m.; $n = 5$ independent experiments (each three coverslips averaged per experiment). In all panels, one-way ANOVA and Bonferroni's *post hoc* tests were used; ns = non-significant ($P > 0.05$). See **Supplementary Figure. 17** for full scans of all western blots for LC3-I, LC3-II, and p62 shown in **n**.

© 2018 Nature America, Inc., part of Springer Nature. All rights reserved.

© 2018 Nature America, Inc., part of Springer Nature. All rights reserved.

that autophagy-dependent cell death of oligodendrocytes was occurring. As reported[54], fibrinogen was not toxic to cultured astrocytes (**Fig. 5r**), which is indicative of differential responses of cell cultures to fibrinogen.

Fibrin fibrils (0.1 mg/ml), prepared and characterized as described in the Online Methods (**Supplementary Fig. 13d**,**e**), were similarly taken up by oligodendrocytes at 6 h (**Supplementary Fig. 13f**). Fibrin fibrils also activated autophagy within 12 h of treatment, as

indicated by an increase in the LC3 II/LC3 I ratio and a decrease in p62 levels (**Fig. 5o**,**p** and **Supplementary Fig. 13g**), and increased caspase 3 activity within 24 h of treatment (**Fig. 5q**) and led to cell death (**Fig. 5r**). MHY1485 blocked the formation of autophagosomes and activation of caspase 3 12 and 24 h after treatment with fibrin fibrils, respectively (**Supplementary Fig. 13c**), which is suggestive of autophagy-dependent cell death. At 24 h after treatment, a relatively low concentration range of fibrin fibrils dose-dependently killed

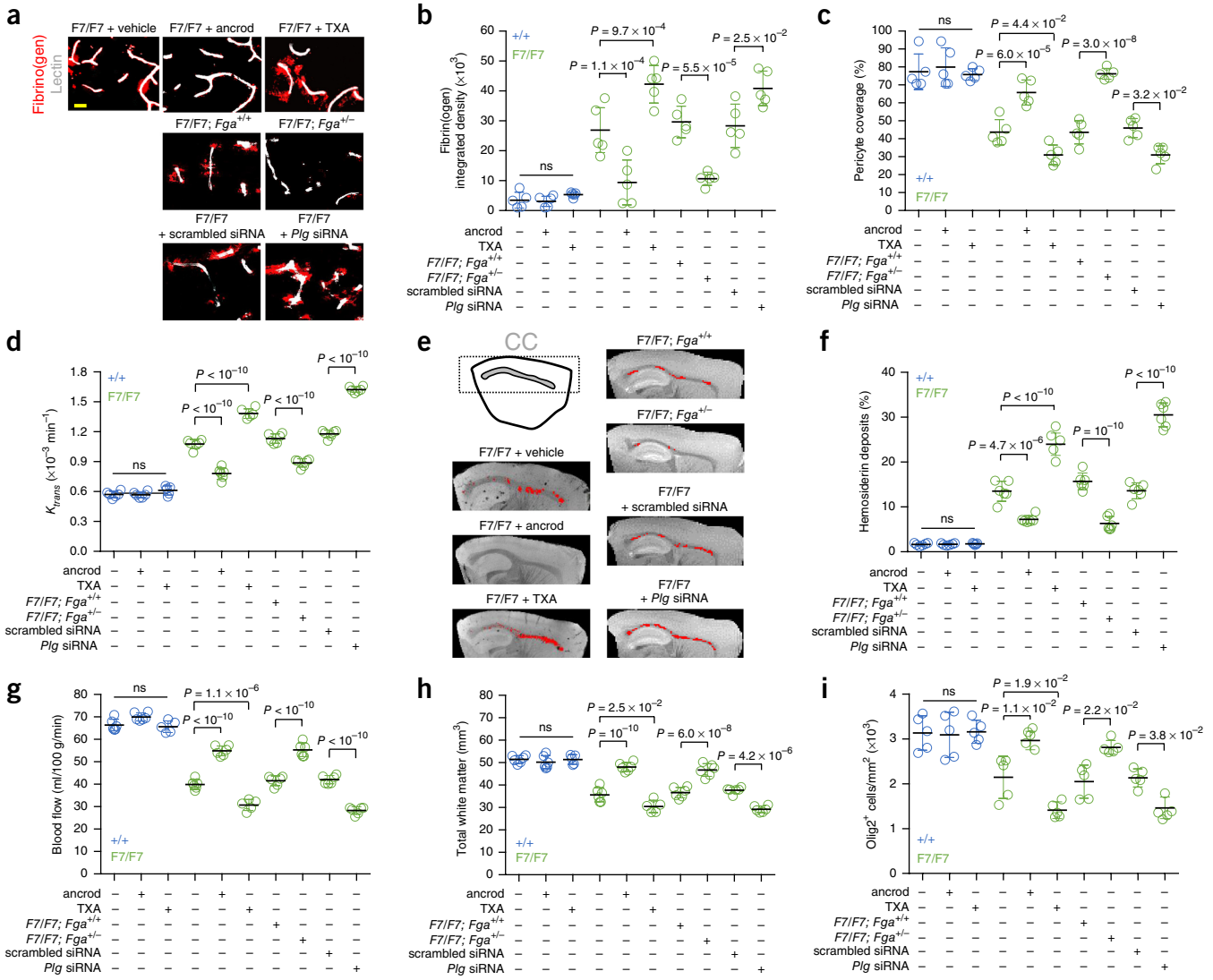

Figure 6 White-matter changes in pericyte-deficient mice after pharmacological or genetic manipulations of systemic fibrinogen levels. (**a**) Extravascular fibrin(ogen) deposits in the CC of 12-week-old F7/F7 mice treated with vehicle, ancrod and TXA (top); or F7/F7 mice crossed with fibrinogen-(*Fga*) deficient +/– mice compared with littermate *Fga*$^{+/+}$ controls (middle); or F7/F7 mice treated with control scrambled siRNA or plasminogen (*Plg*) siRNA for 7 d (bottom), as described in the Online Methods. Scale bar represents 20 μm. (**b**,**c**) Quantification of fibrin(ogen)-positive extravascular deposits (**b**) and CD13-positive pericyte coverage (**c**) in the CC of 12-week-old F7/F7 (green) and control (+/+, blue) mice. Data are presented as mean ± s.d.; $n = 5$ vehicle +/+ and 6 F7/F7 mice; $n = 6$ ancrod-treated +/+ and 5 ancrod-treated F7/F7 mice; $n = 5$ TXA-treated +/+ and F7/F7 mice; $n = 5$ F7/F7; *Fga*$^{+/+}$, F7/F7; *Fga*$^{+/–}$, F7/F7 + scrambled siRNA, and F7/F7 + *Plg* siRNA. (**d**) The K_{trans} capillary permeability constant in the CC of 12-week-old F7/F7 (green) and littermate control (+/+, blue). Values were generated from dynamic contrast-enhanced MRI scans. Data are presented as mean ± s.d.; $n = 6$ vehicle +/+ and F7/F7 mice; $n = 6$ ancrod-treated +/+ and F7/F7 mice; $n = 5$ TXA-treated +/+ and F7/F7 mice; $n = 6$ F7/F7; *Fga*$^{+/+}$, F7/F7; *Fga*$^{+/–}$, F7/F7 + scrambled siRNA, and F7/F7 + *Plg* siRNA. (**e**,**f**) High-resolution T2*-weighted images (sagittal plane) of iron-containing hemosiderin deposits (red dots) in the CC of 12-week-old F7/F7 mice treated with ancrod, TXA or vehicle, crossed with *Fga*$^{+/–}$ compared to littermate *Fga*$^{+/+}$ control mice, and treated with scrambled siRNA or *Plg* siRNA (**e**), and quantification of hemosiderin deposits in the CC of 12-week-old F7/F7 (green) and control (+/+, blue) mice (**f**). Data are presented as mean ± s.d.; $n = 6$ vehicle +/+ and F7/F7 mice; $n = 6$ ancrod-treated +/+ and F7/F7 mice; $n = 5$ TXA-treated +/+ and F7/F7 mice; $n = 6$ F7/F7; *Fga*$^{+/+}$, F7/F7; *Fga*$^{+/–}$, F7/F7 + scrambled siRNA, and F7/F7 + *Plg* siRNA. (**g**) The blood flow values in the CC of 12-week-old F7/F7 (green) and littermate control (+/+, blue) mice generated from dynamic susceptibility-contrast MRI scans. Data are presented as mean ± s.d.; $n = 6$ vehicle +/+ and F7/F7 mice; $n = 6$ ancrod-treated +/+ and F7/F7 mice; $n = 5$ TXA-treated +/+ and F7/F7 mice; $n = 6$ F7/F7; *Fga*$^{+/+}$, F7/F7; *Fga*$^{+/–}$, F7/F7 + scrambled siRNA, and F7/F7 + *Plg* siRNA. (**h**) Total white-matter volume in the CC of 12-week-old F7/F7 (green) and littermate control (+/+, blue) mice. Values were generated from diffusion tensor imaging MRI scans. Data are presented as mean ± s.d.; $n = 6$ vehicle +/+ and F7/F7 mice; $n = 6$ ancrod-treated +/+ and F7/F7 mice; $n = 5$ TXA-treated +/+ and F7/F7 mice; $n = 6$ F7/F7; *Fga*$^{+/+}$, F7/F7; *Fga*$^{+/–}$, F7/F7 + scrambled siRNA, and F7/F7 + *Plg* siRNA. (**i**) Quantification of Olig2-positive cells in the CC of 12-week-old F7/F7 (green) and littermate control (+/+, blue) mice. Data are presented as mean ± s.d.; $n = 5$ mice per group. All data were compared by one-way ANOVA and Bonferroni's *post hoc*; ns = non-significant ($P > 0.05$).

© 2018 Nature America, Inc., part of Springer Nature. All rights reserved.

mature oligodendrocytes (**Supplementary Fig. 13h**). The addition of fibrin fibrils did not interfere with oxygen delivery to cells and/or cellular uptake from the medium, as shown by Image-iT hypoxia probe and Alexa 594-transferrin cellular uptake assay, respectively (**Supplementary Fig. 14a–d**), both of which indicated no change as compared to vehicle-treated controls.

Pericytes are also highly susceptible to cellular stress by various endogenous and exogenous toxins[12,14] including amyloid-β, which can lead to pericyte cell death following intracellular accumulation[55]. Consistent with these findings, we found that cultured mouse pericytes accumulated soluble fibrinogen and fibrin fibrils, which initially activated autophagy, as indicated by the appearance of autophagosomes, but did not activate caspase 3 and/or kill pericytes at early stages; however, at a later stage, such as within 24 h of treatment, both fibrinogen and fibrin fibrils led to activation of caspase 3 in pericytes and to cell death, which was blocked by autophagy inhibitors MHY1485 or autophagy inhibitor VII (**Supplementary Fig. 13i–l**), suggestive of autophagy-dependent cell death.

We next treated 12–16-week-old F7/F7 mice with ancrod (the snake venom enzyme), which has been shown to reduce fibrinogen brain levels in mouse models of multiple sclerosis[47] and AD[41], both of which exhibit BBB breakdown. Compared with vehicle, ancrod substantially reduced fibrinogen plasma levels (**Supplementary Fig. 15a**) and fibrin(ogen) white-matter deposits (**Fig. 6a**,**b**), which was associated with improved pericyte coverage in corpus callosum (**Fig. 6c**), improvement in the blood-axon barrier integrity to circulating MRI tracer gadolinium (**Fig. 6d**), substantial reduction in white-matter hemosiderin deposits (**Fig. 6d–f**) and improvement in blood flow (**Fig. 6g**).

MRI analysis revealed large structural improvements in the white matter of ancrod-treated compared with vehicle-treated F7/F7 mice, including recovery of the white-matter volume (**Fig. 6h**) and normalized fractional anisotropy (**Supplementary Fig. 15b**) and mean diffusivity value (**Supplementary Fig. 15c**). This was associated with increased numbers of Olig2-positive cells (**Fig. 6i**), decreased numbers of TUNEL-positive mature oligodendrocytes[31] (**Supplementary Fig. 15g**,**h**), increased numbers of Olig2 and CNPase double-positive mature oligodendrocytes (**Supplementary Fig. 15i**), and no change in the number of Olig2 and PDGFRα double-positive OPCs[31] (**Supplementary Fig. 15j**). These data suggest that lowering systemic fibrinogen levels improves the function of mature oligodendrocyte pool, but does not affect OPC pools *in vivo*. We also found reduced loss of MBP (**Supplementary Fig. 15d**,**e**) and SMI-312 axon neurofilament staining (**Supplementary Fig. 15d**,**f**).

We then treated 12–16-week-old F7/F7 mice with plasmin-inhibitor tranexamic acid (TXA), which leads to increased fibrin(ogen) deposition in the brain in animal models with pre-existing brain vascular lesions, such as AD mice[41]. TXA increased plasma fibrinogen levels (**Supplementary Fig. 15a**) and white-matter fibrin(ogen) deposits (**Fig. 6a**,**b**) compared with vehicle in F7/F7 mice with disrupted BBB, but not in littermate controls with intact BBB. Consistent with neurovascular toxicity of fibrin(ogen) *in vivo*[41] and toxicity of soluble fibrinogen and fibrin fibrils to cultured pericytes (**Supplementary Fig. 13i–l**), TXA treatment accelerated the loss of pericyte coverage in the white-matter microvessels (**Fig. 6c**) and the blood-axon barrier breakdown (**Fig. 6d**), increased the number of hemosiderin deposits (**Fig. 6c**,**d**), and reduced white-matter blood flow (**Fig. 6e**). As expected, MRI analysis revealed a greater loss of white-matter volume (**Fig. 6h**), lower fractional anisotropy (**Supplementary Fig. 15b**) and increased mean diffusivity (**Supplementary Fig. 15c**), indicative of augmented white-matter damage. Immunostaining for Olig2, MBP and SMI-312 revealed an accelerated loss of Olig2-positive oligodendrocytes (**Fig. 6i**), myelin (**Supplementary Fig. 15d**,**e**) and axon degeneration (**Supplementary Fig. 15d**,**f**), respectively. Triple immunostaining for TUNEL, Olig2 and CNPase revealed an increase in TUNEL-positive mature oligodendrocytes in TXA-treated compared with vehicle-treated F7/F7 mice (**Supplementary Fig. 15g**,**h**), which was associated with reduced number of Olig2 and CNPase double-positive mature oligodendrocytes (**Supplementary Fig. 15i**), but did not influence the number of OPCs (**Supplementary Fig. 15j**). These data indicate that increasing systemic fibrinogen levels kills mature oligodendrocytes, but does not affect OPC pools. Neither ancrod nor TXA treatment influenced white-matter fibrin(ogen) levels in control animals with intact BBB (**Fig. 6b**), and neither ancrod nor TXA were directly toxic to cultured oligodendrocytes and pericytes (not shown).

To confirm our findings with pharmacological inhibitors, we used fibrinogen alpha-chain (encoded by *Fga* gene) deficient mice[56] crossed with F7/F7 mice. These fibrinogen-deficient mice have been used to study the role of fibrinogen deficiency on defects in the AD mouse BBB[41] and in an experimental autoimmune encephalitis model[57]. We found that F7/F7 $Fga^{+/-}$ mice, as compared with F7/F7 $Fga^{+/+}$ littermate controls, developed substantial reductions in fibrinogen plasma levels (**Supplementary Fig. 15a**) and fibrin(ogen) white-matter deposits (**Fig. 6a**,**b**). This was associated with improvements in pericyte coverage (**Fig. 6c**) and the blood-axon barrier integrity (**Fig. 6d**), substantial reductions in hemosiderin deposits (**Fig. 6f**), improvements in blood flow (**Fig. 6g**), recovery in the white matter volume (**Fig. 6h**), and normalized fractional anisotropy (**Supplementary Fig. 15b**) and mean diffusivity (**Supplementary Fig. 15c**). Tissue analysis confirmed an increase in the number of oligodendrocytes (**Fig. 6i**) and a reduction in the amount of MBP loss (**Supplementary Fig. 15d**,**e**) and SMI-312 axon neurofilament staining (**Supplementary Fig. 15d**,**f**) compared with littermate controls.

To genetically knock down plasminogen (encoded by *Plg* gene), we employed small interfering RNA (siRNA) to short-term silence *Plg* expression, which has been shown to effectively downregulate gene expression *in vivo* through the RNA-induced silencing complex[58]. Given that Plg is expressed mainly in the liver, but is also detectable in the brain, we performed both siRNA systemic administration via tail vein injection and central administration by bilateral intracerebroventricular injection (Online Methods). The knockdown efficiency of *Plg*-specific siRNA compared with scrambled siRNA was confirmed by quantitative reverse-transcription PCR and western blot analysis (**Supplementary Fig. 16a–d**), and we observed substantially lower plasminogen plasma levels in control and F7/F7 mice (**Supplementary Fig. 16e**,**f**).

Treatment of F7/F7 mice with *Plg* siRNA, as compared with scrambled siRNA, considerably increased fibrinogen plasma levels (**Supplementary Fig. 15a**) and white-matter fibrin(ogen) accumulation (**Fig. 6a**,**b**), which was associated with increased loss of white-matter pericyte coverage, (**Fig. 6c**), accelerated blood-axon barrier breakdown (**Fig. 6d**), increased hemosiderin deposits (**Fig. 6f**) and reduced white-matter blood flow (**Fig. 6e**). Accelerated vascular pathology led to a greater loss of white-matter volume (**Fig. 6h**), lower fractional anisotropy (**Supplementary Fig. 15b**) and increased mean diffusivity (**Supplementary Fig. 15c**), indicative of greater white-matter damage. Immunostaining for Olig2, MBP and SMI-312 revealed accelerated loss of Olig2-positive oligodendrocytes (**Fig. 6i**), myelin (**Supplementary Fig. 15d**,**e**) and axon degeneration (**Supplementary Fig. 15d**,**f**).

© 2018 Nature America, Inc., part of Springer Nature. All rights reserved.

© 2018 Nature America, Inc., part of Springer Nature. All rights reserved.

DISCUSSION

Our findings demonstrate that pericytes maintain the physiological environment in the white matter, which is required for fully functional neuronal connectivity. We found that pericyte degeneration led to early breakdown of the blood-axon barrier, resulting in early accumulation of blood-derived toxic fibrin(ogen) deposits in the white matter. This was associated with increases in fluid-filled enlarged perivascular spaces and diminished blood flow, leading to white-matter hypoxia in young pericyte-deficient mice (**Supplementary Fig. 18**), at the time when hypoxic changes are undetectable in the cortex and hippocampus. This aggressive white-matter vascular phenotype led to a loss of myelin, axons and oligodendrocytes, causing disruption of neural circuits and white-matter-related functional deficits long before neuronal loss occurred. Given that F7/F7 mice have normal hemodynamic, physiological and biochemical parameters and do not develop a general systemic perfusion deficit and/or an apparent cardiovascular insufficiency, as previously reported[17], we can conclude that the white-matter vascular phenotype is mainly of local character.

By pharmacologically or genetically manipulating systemic fibrinogen levels, we found that lowering plasma fibrinogen reduced the degree of white-matter fibrin(ogen) deposits, pericyte degeneration, vascular pathology and white-matter degeneration, whereas increasing plasma fibrinogen had the opposite effects. These data suggest that accumulation of white-matter fibrin(ogen) provides an important pathogenic link to pericyte loss, microvascular dysfunction, white matter pathology and oligodendrocyte loss. Consistent with these data, we also found that oligodendrocyte and pericyte cultures were highly vulnerable to soluble fibrinogen and fibrin fibrils *in vitro*, such that either independently triggered autophagy-dependent cell death when added to the culture medium. In contrast, astrocytes remained unaffected, as previously shown[54]. These data suggest that fibrinogen and fibrin may exert differential cell-specific effects, but their effects could also be influenced by experimental conditions, such as whether cells were cultured on fibrin-coated matrices, as opposed to adding fibrin fibrils to the culture medium.

In contrast with previous studies demonstrating that fibrin promotes neuroinflammation and microglia activation in animal models of AD[41] and multiple sclerosis[47] and stimulates activation and induction of antigen-presenting genes in primary microglia and bone-marrow-derived macrophages[45], we failed to detect changes in the number of white-matter astrocytes and microglia in 4–48-week-old F7/F7 mice (**Supplementary Fig. 19a–h**) or changes in cytokine and chemokine expression levels (**Supplementary Fig. 19i**). Our data are consistent, however, with previous findings in pericyte-deficient mice showing no changes in astrocyte, microglia and macrophage responses after white-matter injury, or changes in pro-inflammatory and anti-inflammatory cell profiles[59] and/or numbers of astrocytes and microglia at the resting state[17]. Pericytes can also interact with different cell types, such as supporting OPC differentiation into oligodendrocytes, as shown in cultures *in vitro*, but do not influence remyelination from OPCs *in vivo*, as shown in pericyte-deficient mice with diminished platelet-derived growth factor-BB bioavailability after spinal cord white-matter injury[59].

Despite a lack of direct evidence supporting a relationship between age-dependent white-matter disease and *PDGFRB* deficiency in humans[14], a recent study found that $PDGFRB^{Pro584Arg}$ point mutation leads to a rare human disease with a complex syndrome, including neurological deterioration and extensive white matter lesions[60]. This study did not attempt to elucidate, however, whether white-matter lesions in these $PDGFRB^{Pro584Arg}$ carriers were caused by pericyte degeneration or not.

In summary, our findings indicate that pericytes have an important role in white-matter health and disease. We found that pericyte degeneration leads to phenotypic changes in mice similar to those described in the white-matter disease associated with small-vessel disease contributing to dementia in humans[1–4]. In addition, neurological disorders associated with cognitive impairment, cerebrovascular dysfunction and white matter lesions, including AD[23–26], mild dementia[27], stroke[14,16] and CADASIL[28], exhibit pericyte degeneration, including loss of pericyte coverage in the white matter, as we found in AD. Thus, our findings may have important implications for the pathogenesis and treatment of small-vessel disease and age-related white-matter disease, and suggest pericytes as a trigger, and potential therapeutic target, for white-matter disease.

METHODS

Methods, including statements of data availability and any associated accession codes and references, are available in the online version of the paper.

Note: Any Supplementary Information and Source Data files are available in the online version of the paper.

ACKNOWLEDGMENTS

This research was supported by US National Institute of Health grants NS100459, AG039452, NS034467 and AG023084 to B.V.Z., the Foundation Leducq Transatlantic Network of Excellence for the Study of Perivascular Spaces in Small Vessel Disease reference no. 16 CVD 05, and ES024936 to W.J.M. The authors thank M.T. Huuskonen for assistance with MRI scanning sessions.

AUTHOR CONTRIBUTIONS

A.M., A.M.N. and Z.Z. designed and performed experiments, analyzed data and contributed to the writing of the paper. A.P.S., G.S., D.L., S.R.B., M.D., A.R., A.G., E.J.L., Y.W., J.V., M.H. and R.L. performed experiments and analyzed data. W.J.M., P.M.T., J.A.S., R.E.J. and E.M. provided guidance for some experiments and edited the paper. B.V.Z. designed all of the experiments and wrote the paper.

COMPETING FINANCIAL INTERESTS

The authors declare no competing financial interests.

Reprints and permissions information is available online at http://www.nature.com/reprints/index.html. Publisher's note: Springer Nature remains neutral with regard to jurisdictional claims in published maps and institutional affiliations.

1. Wardlaw, J.M. *et al.* Neuroimaging standards for research into small vessel disease and its contribution to ageing and neurodegeneration. *Lancet Neurol.* **12**, 822–838 (2013).
2. Iadecola, C. The pathobiology of vascular dementia. *Neuron* **80**, 844–866 (2013).
3. Snyder, H.M. *et al.* Vascular contributions to cognitive impairment and dementia including Alzheimer's disease. *Alzheimers Dement.* **11**, 710–717 (2015).
4. Hachinski, V. & World Stroke Organization. Stroke and potentially preventable dementias proclamation: updated World Stroke Day Proclamation. *Stroke J. Cereb. Circ.* **46**, 3039–3040 (2015).
5. Phillips, O.R. *et al.* The superficial white matter in Alzheimer's disease. *Hum. Brain Mapp.* **37**, 1321–1334 (2016).
6. Lee, S. *et al.* White matter hyperintensities are a core feature of Alzheimer's disease: evidence from the dominantly inherited Alzheimer network. *Ann. Neurol.* **79**, 929–939 (2016).
7. Behrendt, G. *et al.* Dynamic changes in myelin aberrations and oligodendrocyte generation in chronic amyloidosis in mice and men. *Glia* **61**, 273–286 (2013).
8. Schuff, N. *et al.* Cerebral blood flow in ischemic vascular dementia and Alzheimer's disease, measured by arterial spin-labeling magnetic resonance imaging. *Alzheimers Dement.* **5**, 454–462 (2009).
9. Hanaoka, T. *et al.* Relationship between white matter lesions and regional cerebral blood flow changes during longitudinal follow up in Alzheimer's disease. *Geriatr. Gerontol. Int.* **16**, 836–842 (2016).
10. Miners, J.S., Schulz, I. & Love, S. Differing associations between Aβ accumulation, hypoperfusion, blood-brain barrier dysfunction and loss of PDGFRB pericyte marker in the precuneus and parietal white matter in Alzheimer's disease. *J. Cereb. Blood Flow Metab.* **38**, 103–115 (2017).
11. Arvanitakis, Z., Capuano, A.W., Leurgans, S.E., Bennett, D.A. & Schneider, J.A. Relation of cerebral vessel disease to Alzheimer's disease dementia and cognitive function in elderly people: a cross-sectional study. *Lancet Neurol.* **15**, 934–943 (2016).

12. Zhao, Z., Nelson, A.R., Betsholtz, C. & Zlokovic, B.V. Establishment and dysfunction of the blood-brain barrier. *Cell* **163**, 1064–1078 (2015).
13. Attwell, D., Mishra, A., Hall, C.N., O'Farrell, F.M. & Dalkara, T. What is a pericyte? *J. Cereb. Blood Flow Metab.* **36**, 451–455 (2016).
14. Sweeney, M.D., Ayyadurai, S. & Zlokovic, B.V. Pericytes of the neurovascular unit: key functions and signaling pathways. *Nat. Neurosci.* **19**, 771–783 (2016).
15. Daneman, R., Zhou, L., Kebede, A.A. & Barres, B.A. Pericytes are required for blood-brain barrier integrity during embryogenesis. *Nature* **468**, 562–566 (2010).
16. Armulik, A. *et al.* Pericytes regulate the blood-brain barrier. *Nature* **468**, 557–561 (2010).
17. Bell, R.D. *et al.* Pericytes control key neurovascular functions and neuronal phenotype in the adult brain and during brain aging. *Neuron* **68**, 409–427 (2010).
18. Peppiatt, C.M., Howarth, C., Mobbs, P. & Attwell, D. Bidirectional control of CNS capillary diameter by pericytes. *Nature* **443**, 700–704 (2006).
19. Hall, C.N. *et al.* Capillary pericytes regulate cerebral blood flow in health and disease. *Nature* **508**, 55–60 (2014).
20. Yemisci, M. *et al.* Pericyte contraction induced by oxidative-nitrative stress impairs capillary reflow despite successful opening of an occluded cerebral artery. *Nat. Med.* **15**, 1031–1037 (2009).
21. Mishra, A. *et al.* Astrocytes mediate neurovascular signaling to capillary pericytes but not to arterioles. *Nat. Neurosci.* **19**, 1619–1627 (2016).
22. Kisler, K. *et al.* Pericyte degeneration leads to neurovascular uncoupling and limits oxygen supply to brain. *Nat. Neurosci.* **20**, 406–416 (2017).
23. Farkas, E. & Luiten, P.G. Cerebral microvascular pathology in aging and Alzheimer's disease. *Prog. Neurobiol.* **64**, 575–611 (2001).
24. Baloyannis, S.J. & Baloyannis, I.S. The vascular factor in Alzheimer's disease: a study in Golgi technique and electron microscopy. *J. Neurol. Sci.* **322**, 117–121 (2012).
25. Sengillo, J.D. *et al.* Deficiency in mural vascular cells coincides with blood-brain barrier disruption in Alzheimer's disease. *Brain Pathol.* **23**, 303–310 (2013).
26. Halliday, M.R. *et al.* Accelerated pericyte degeneration and blood-brain barrier breakdown in apolipoprotein E4 carriers with Alzheimer's disease. *J. Cereb. Blood Flow Metab.* **36**, 216–227. (2016).
27. Montagne, A. *et al.* Blood-brain barrier breakdown in the aging human hippocampus. *Neuron* **85**, 296–302 (2015).
28. Ghosh, M. *et al.* Pericytes are involved in the pathogenesis of cerebral autosomal dominant arteriopathy with subcortical infarcts and leukoencephalopathy. *Ann. Neurol.* **78**, 887–900 (2015).
29. Tallquist, M.D., French, W.J. & Soriano, P. Additive effects of PDGF receptor β signaling pathways in vascular smooth muscle cell development. *PLoS Biol.* **1**, E52 (2003).
30. Nikolakopoulou, A.M., Zhao, Z., Montagne, A. & Zlokovic, B.V. Regional early and progressive loss of brain pericytes but not vascular smooth muscle cells in adult mice with disrupted platelet-derived growth factor receptor-β signaling. *PLoS One* **12**, e0176225 (2017).
31. Baumann, N. & Pham-Dinh, D. Biology of oligodendrocyte and myelin in the mammalian central nervous system. *Physiol. Rev.* **81**, 871–927 (2001).
32. Winkler, E.A., Bell, R.D. & Zlokovic, B.V. Pericyte-specific expression of PDGΦβ receptor in mouse models with normal and deficient PDGFβ receptor signaling. *Mol. Neurodegener.* **5**, 32 (2010).
33. Bell, R.D. *et al.* Apolipoprotein E controls cerebrovascular integrity via cyclophilin A. *Nature* **485**, 512–516 (2012).
34. Daianu, M. *et al.* 7T multi-shell hybrid diffusion imaging (HYDI) for mapping brain connectivity in mice. *Proc. SPIE–Int. Soc. Opt. Eng.* **9413**, 941309 (2015).
35. Zingg, B. *et al.* Neural networks of the mouse neocortex. *Cell* **156**, 1096–1111 (2014).
36. Potter, G.M. *et al.* Enlarged perivascular spaces and cerebral small vessel disease. *Int. J. Stroke* **10**, 376–381 (2015).
37. Trapp, B.D. & Nave, K.-A. Multiple sclerosis: an immune or neurodegenerative disorder? *Annu. Rev. Neurosci.* **31**, 247–269 (2008).
38. Pohl, H.B.F. *et al.* Genetically induced adult oligodendrocyte cell death is associated with poor myelin clearance, reduced remyelination, and axonal damage. *J. Neurosci.* **31**, 1069–1080 (2011).
39. Dewar, D., Underhill, S.M. & Goldberg, M.P. Oligodendrocytes and ischemic brain injury. *J. Cereb. Blood Flow Metab.* **23**, 263–274 (2003).
40. Rosenzweig, S. & Carmichael, S.T. Age-dependent exacerbation of white matter stroke outcomes: a role for oxidative damage and inflammatory mediators. *Stroke* **44**, 2579–2586 (2013).
41. Paul, J., Strickland, S. & Melchor, J.P. Fibrin deposition accelerates neurovascular damage and neuroinflammation in mouse models of Alzheimer's disease. *J. Exp. Med.* **204**, 1999–2008 (2007).
42. Cortes-Canteli, M. *et al.* Fibrinogen and β-amyloid association alters thrombosis and fibrinolysis: a possible contributing factor to Alzheimer's disease. *Neuron* **66**, 695–709 (2010).
43. Cortes-Canteli, M., Mattei, L., Richards, A.T., Norris, E.H. & Strickland, S. Fibrin deposited in the Alzheimer's disease brain promotes neuronal degeneration. *Neurobiol. Aging* **36**, 608–617 (2015).
44. Schachtrup, C. *et al.* Fibrinogen inhibits neurite outgrowth via β3-integrin-mediated phosphorylation of the EGF receptor. *Proc. Natl. Acad. Sci. USA* **104**, 11814–11819 (2007).
45. Ryu, J.K. *et al.* Blood coagulation protein fibrinogen promotes autoimmunity and demyelination via chemokine release and antigen presentation. *Nat. Commun.* **6**, 8164 (2015).
46. Akassoglou, K., Yu, W.M., Akpinar, P. & Strickland, S. Fibrin inhibits peripheral nerve remyelination by regulating Schwann cell differentiation. *Neuron* **33**, 861–875 (2002).
47. Akassoglou, K. *et al.* Fibrin depletion decreases inflammation and delays the onset of demyelination in a tumor necrosis factor transgenic mouse model for multiple sclerosis. *Proc. Natl. Acad. Sci. USA* **101**, 6698–6703 (2004).
48. Adams, R.A. *et al.* The fibrin-derived γ377-395 peptide inhibits microglia activation and suppresses relapsing paralysis in central nervous system autoimmune disease. *J. Exp. Med.* **204**, 571–582 (2007).
49. Altman, B.J. & Rathmell, J.C. Metabolic stress in autophagy and cell death pathways. *Cold Spring Harb. Perspect. Biol.* **4**, a008763 (2012).
50. Mizushima, N., Yoshimori, T. & Levine, B. Methods in mammalian autophagy research. *Cell* **140**, 313–326 (2010).
51. McIlwain, D.R., Berger, T. & Mak, T.W. Caspase functions in cell death and disease. *Cold Spring Harb. Perspect. Biol.* **5**, a008656 (2013).
52. Choi, Y.J. *et al.* Inhibitory effect of mTOR activator MHY1485 on autophagy: suppression of lysosomal fusion. *PLoS One* **7**, e43418 (2012).
53. Wang, T. *et al.* Synthesis of improved lysomotropic autophagy inhibitors. *J. Med. Chem.* **58**, 3025–3035 (2015).
54. Schachtrup, C. *et al.* Fibrinogen triggers astrocyte scar formation by promoting the availability of active TGF-β after vascular damage. *J. Neurosci.* **30**, 5843–5854 (2010).
55. Sagare, A.P. *et al.* Pericyte loss influences Alzheimer-like neurodegeneration in mice. *Nat. Commun.* **4**, 2932 (2013).
56. Suh, T.T. *et al.* Resolution of spontaneous bleeding events but failure of pregnancy in fibrinogen-deficient mice. *Genes Dev.* **9**, 2020–2033 (1995).
57. Shaw, M.A. *et al.* Plasminogen deficiency delays the onset and protects from demyelination and paralysis in autoimmune neuroinflammatory disease. *J. Neurosci.* **37**, 3776–3788 (2017).
58. Wittrup, A. & Lieberman, J. Knocking down disease: a progress report on siRNA therapeutics. *Nat. Rev. Genet.* **16**, 543–552 (2015).
59. De La Fuente, A.G. *et al.* Pericytes stimulate oligodendrocyte progenitor cell differentiation during CNS remyelination. *Cell Rep.* **20**, 1755–1764 (2017).
60. Takenouchi, T. *et al.* Novel overgrowth syndrome phenotype due to recurrent *de novo PDGFRB* mutation. *J. Pediatr.* **166**, 483–486 (2015).

© 2018 Nature America, Inc., part of Springer Nature. All rights reserved.

ONLINE METHODS

Human postmortem studies. *Tissue samples*. Post-mortem paraffin embedded human brain samples (Brodmann area 9/10, with subcortical white matter) were obtained from the Rush University Medical Center and the University of Southern California, as we previously described[61]. Informed consent was obtained and the study approved by the Institutional Review Board of Rush University Medical Center and the University of Southern California. All autopsy cases underwent neuropathological evaluation of AD including assignment of Braak stages. Aged subjects that did not carry diagnosis of AD or another neurodegenerative disease and showed neuropathological findings within the normal range for age were used as age-matched controls. Mini-Mental State Examination information was available for most but not all individuals. A total of 15 controls and 16 AD individuals were used for histopathological analyses. The demographic information of all cases is provided in **Supplementary Table 1**. All procedures performed in this manuscript were in accordance with the ethical standards of both Rush University Medical Center and University of Southern California.

Histopathological analyses. All analyses on human tissue were performed as we previously described[61]. Heat-induced antigen retrieval was performed following Dako's protocol. For immunofluorescence analysis, we used the following primary antibodies: for pericyte coverage, polyclonal goat anti-human PDGFRβ (R&D systems, AF385; 1:100); for fibrinogen and fibrin extravascular deposits, polyclonal rabbit anti-human fibrinogen (Dako, A0080; 1:500); and species-specific fluorochrome-conjugated secondary antibodies were incubated (see **Supplementary Table 2**) for 1 h at 19–23 °C. Blood vessel endothelial profiles were stained by Dylight 488-conjugated *L. esculentum* lectin (Vector Labs, DL-1174; 1:200) for 1 h at 19–23 °C. All slices were scanned using Zeiss 510 confocal microscope with Zeiss Apochromat water immersion objectives (Carl Zeiss MicroImaging).

Animals. Platelet-derived growth factor receptor β mutant mice, *Pdgfrb*$^{F7/F7}$ (F7/F7), were generated by point mutations that disrupt the following residues and designated signal transduction pathways; residue 578 (Src), residue 715 (Grb2), residues 739 and 750 (PI3K), residue 770 (RasGAP), residue 1008 (SHP-2), by changing the tyrosine to phenylalanine, and residue 1020 (PLCγ), where tyrosine was mutated to isoleucine[29]. F7/F7 mice were maintained on a 129S1/SvlmJ background and were shown to express PDGFRβ in the brain exclusively in perivascular mural cells including pericytes, and not in neurons, astrocytes or endothelial cells[17,32]. Because previous studies in mice with deficient PDGFRβ signaling did not find the effect of gender on pericyte coverage, BBB integrity or blood flow regulation[17,22,30,32], both male and female mice at 2, 4–6, 12–16 and 36–48 weeks of age were used in the study. To determine the role for fibrinogen in F7/F7 mice we carried out pharmacological studies with ancrod and TXA and genetic studies using fibrinogen-deficient and plasminogen-deficient mice, as described below. All procedures were approved by the Institutional Animal Care and Use Committee at the University of Southern California using US National Institutes of Health guidelines. All animals were randomized for their genotype information and were included in the study. The operators responsible for experimental procedure and data analysis were blinded and unaware of group allocation throughout the experiments.

Pharmacological studies with ancrod and TXA. For fibrinogen depletion experiments, ancrod- or saline-filled mini-pumps (Alzet, Mini-osmotic pump, Model 2002) were implanted in the back of 12-week-old F7/F7 and age-matched control (+/+) littermate mice. Ancrod (NIBSC, cat #74-581; 55 IU/ampoule; total volume 250 μl) was delivered at a rate of 0.52 μl/h or approximately 2.75 IU/d for 14 d. After 14 d, animals were used for MRI studies, and then sacrificed for immunocytochemistry studies, as described below.

Deficiency in fibrinolysis was accomplished pharmacologically in 12-week-old F7/F7 and control (+/+) mice by intraperitoneal (i.p.) injections of TXA (#1672745, Sigma-Aldrich), as reported[41]. We used a 3-d protocol with approximately 6,500 mg TXA/kg/d i.p. (200 mg daily per mouse), which was comparable to TXA protocol recommended for humans undergoing cardiac surgery. Animals also received TXA dissolved in drinking water at 25 mg/ml, as previously reported[41]. Previous studies in AD mice used somewhat lower dose of TXA (approximately 100 mg per mouse), but for longer periods of time of 14 d[41]. After 3 d, animals were used for MRI studies, and then sacrificed for immunohistochemistry studies, as described below.

Studies with fibrinogen-deficient and plasminogen-deficient mice. To genetically lower fibrinogen levels in F7/F7 mice, fibrinogen alpha chain (encoded by *Fga* gene) deficient heterozygous mice (*Fga*$^{+/-}$)[56] maintained on a mixed genetic background were crossed with F7/F7 mice. Double transgenic F7/F7; *Fga*$^{+/-}$ mice and their F7/F7; *Fga*$^{+/+}$ littermate controls were compared and used for MRI studies at 12–16 weeks of age, and then sacrificed for immunocytochemistry studies, as described below. To genetically lower plasminogen (encoded by *Plg* gene) levels we used small interfering RNA (siRNA)[58] in 12–16-week-old F7/F7 mice. F7/F7 mice were treated with either *Plg* siRNA or scrambled siRNA, and were used for MRI studies 7 d after treatment, and then sacrificed for immunocytochemistry studies, as described below.

siRNA gene silencing. To knockdown Plg in F7/F7 mice, we used *Plg*-specific chemically modified, 21-mer, double-stranded Ambion *In vivo* siRNA (ThermoFisher), which has superior effectiveness and stability *in vivo* and can effectively suppress gene expression within 24 h with the effect lasting for more than two weeks after a single injection when used with Invivofectamine reagent. Since Plg is expressed mainly in the liver, but is also detectable in the brain[62], we performed both systemic administration via tail vein injection and central administration by bilateral intracerebroventricular injection[63]. Ambion *In vivo* siRNA was reconstituted in Invivofectamine 3.0 reagent and diluted in PBS; a final dose of 1.5 nmol (equivalent to 1 mg/kg) in 100 μL was used for tail vein injection, and a final dose of 0.1 nmol in 1 μl was delivered to both ventricles using a Hamilton syringe over 5 min. The knockdown efficiency of *Plg*-specific siRNA compared to scrambled siRNA was confirmed by quantitative reverse-transcription PCR and western blot analysis, which indicated 82% and 95% inhibition of *Plg* mRNA and protein levels in the liver, respectively, and 81% inhibition of *Plg* mRNA in the brain, whereas Plg protein was undetectable in the brain (**Supplementary Fig. 16a–d**).

Fibrinogen and plasminogen plasma levels. Mouse plasma fibrinogen levels were determined by mouse fibrinogen enzyme-linked immunosorbent assay (ELISA) kit (Immunology Consultants Laboratory, E-90FIB). Blood was collected in EDTA before cardiac perfusion via cardiac puncture. Plasma was separated by centrifugation at 2,000 g for 10 min. Plasma fibrinogen concentrations are given in mg/ml for a plasma dilution of 1:20,000. Mouse plasma plasminogen levels were determined by mouse plasminogen ELISA kit (Immunology Consultants Laboratory, E-90PMG). Plasma plasminogen concentrations are given in μg/ml for a plasma dilution of 1:5,000.

Magnetic resonance imaging. *In vivo* MRI. F7/F7 mice and littermate controls were scanned with a Biospec 7T system (300 MHz, Bruker) at the California Institute of Technology. The magnet is equipped with the standard B-GA12 gradient set (~12-mm inner diameter; 400 mT m^{-1} maximum gradient) and a 35-mm internal diameter quadrature volume coil was used (M2M Imaging). Fibrinogen-deficient and plasminogen-deficient F7/F7 mice and their littermate controls were scanned with our new MR Solutions 7T PET-MR system (MR Solutions) at the Zilkha Neurogenetic Institute (University of Southern California). The MR Solutions magnet is equipped with the MRS cryogen-free MRI system (bore size ~24-mm, up to 600 mT m^{-1} maximum gradient) and a 20-mm internal diameter quadrature bird cage mouse head coil. Comparable sequences and parameters were used with both MR scanners, as described below.

Mice were anesthetized by 1–1.5% isoflurane/air. Respiration rate (80–120 breaths per min) and body temperature (36.5 ± 0.5 °C) are monitored during the experiments using an abdominal pressure-sensitive probe and a rectal temperature probe. The isoflurane dose and heated air flow was adjusted continuously to ensure stable and reproducible depth of anesthesia. The sequences are collected in the following order: diffusion tensor imaging (2D-echo planar imaging (EPI), TR/TE 5,000/28 ms, 30 directions, b-value 670 s/mm^2, diffusion gradient duration/separation 5/10 ms, resolution 170 × 170 × 750 μm^3) to study structural white-matter changes; T2*-weighted imaging (3D-gradient echo with flow compensation (GEFC), TR/TE = 32/15 ms, averages 6, flip angle 12°, resolution 80 × 80 × 300 μm^3) to detect hemosiderin deposits; T2-weighted imaging (2D-RARE factor 2, TR/TE = 2,742/11 ms, averages 2, resolution 125 × 100 × 500 μm^3) to obtain structural images; dynamic contrast-enhanced (DCE) protocol for the capillary permeability assessment; and finally, DSC imaging for

© 2018 Nature America, Inc., part of Springer Nature. All rights reserved.

regional blood flow and blood volume measurements. Total imaging time was approximately 1.5 h per mouse.

The DCE-MRI imaging protocol is performed on two brain slices (within the dorsal hippocampus territory and the prefrontal cortex), and includes measurement of pre-contrast T1-values using a variable time repetition (VTR) spin-echo sequence (TR = 5,000, 3,000, 1,500, 800, 400 and 200 ms, RARE factor 3, TE = 11 ms, 1 average, resolution 0.2 × 0.2 × mm^3), followed by a dynamic series of 800 T1-weighted images with identical geometry and a temporal resolution of 2.6 s (fast low angle shot (FLASH), TR/TE = 20.6/3.2 ms, 2 averages, flip angle 15°, 200x200x1000 μm^3). Using a power injector, a bolus dose of 0.5 mmol/kg Gd-DTPA (Gadolinium-diethylenetriamine pentaacetic acid, Magnevist, diluted in saline 1:5) is injected via the tail vein (rate of 600 µl/min) at 5 min (volume injected 140 µl) and DCE images are collected for an additional 30 min after the injection. The DSC-MRI imaging is performed on the exact same geometry. A dynamic series of 160 T2*-weighted images is used, with a temporal resolution of 600 ms (FLASH, TR/TE = 18.9/5 ms, 1 average, flip angle 15°, resolution 200 × 200 × 1,000 μm^3). A second bolus dose of Gd-DTPA (Magnevist; 1:1) is injected via the tail vein (rate of 1,000 µl/min) at 18 s (volume injected 140 µl) and DSC images are collected for an additional 80 s after the injection.

Ex vivo DTI-MRI. An 11.7-T 89-mm vertical bore Bruker BioSpin Avance DRX500 scanner (Bruker BioSpin) equipped with a Micro 2.5 gradient system was used to acquire all diffusion weighted images (DWIs) of the mouse brains. Fixed brains were kept within the skull, all skin and cartilaginous tissue were removed, and brains were soaked at 4 °C in 5 mM Gadolinium contrast ProHance (Bracco Diagnostics) for 4 d before scanning to minimize the T1 relaxation effect on the tissue. For each scan, two intact fixed heads were secured in a Teflon holder, submerged in Galden (perfluoropolyether with same magnetic susceptibility as water) (Fomblin, Solvay Solexis). This ensured that no leakage would occur and that the signal would not change during acquisition in a 20-mm linear birdcage radio frequency (RF) coil. First, 3D-rapid acquisition with relaxation enhancement (RARE) anatomical images were acquired (TR/TE = 250/9 ms; RARE factor 8; 140 × 80 × 80 matrix; 28 × 16 × 16 mm FOV, 200 µm isotropic voxel size; 1 average). Then, DWIs were acquired using a conventional pulsed-gradient spin echo (PGSE) sequence (TR/TE = 300/16.2 ms, 350 × 200 × 200 matrix, 28 × 16 × 16 mm FOV, 80 µm isotropic voxel size, 1 average, δ = 3 ms, Δ = 8 ms, G_d = 1,000 mT/m, nominal b-factor = 3000 s/mm^2). Six diffusion weighted images were acquired in addition to one volume with no diffusion sensitization using an optimized six points icosahedral encoding scheme for a total imaging time of 24 h.

Ex vivo T2*-weighted-MRI. An 11.7-T 89-mm vertical bore Bruker BioSpin Avance DRX500 scanner (Bruker BioSpin) equipped with a Micro 2.5 gradient system was used to acquire high resolution T2*-weighted images. Fixed brains were kept within the skull, all skin and cartilaginous tissue were removed, and brains were soaked at 4 °C in 2 mM Gadolinium contrast ProHance (Bracco Diagnostics) for 2 d before scanning to minimize the T1 relaxation effect on the tissue. For each scan, two intact fixed heads were secured in a Teflon holder, submerged in Galden (perfluoropolyether with same magnetic susceptibility as water) (Fomblin, Solvay Solexis). This ensured that no leakage would occur and that the signal would not change during acquisition in a 20-mm linear birdcage radio frequency (RF) coil. First, 3D-rapid acquisition with relaxation enhancement (RARE) anatomical images were acquired (TR/TE = 250/9 ms; RARE factor 8; 140 × 80 × 80 matrix; 28 × 16 × 16 mm FOV, 200 µm isotropic voxel size; 1 average). Then, high-resolution T2*-weighted images were acquired using a FLASH sequence (TR/TE = 50/5.19 ms, 400 × 200 × 240 matrix, 28 × 16 × 16 mm FOV, 50 µm isotropic voxel size, averages 18) for a total imaging scan of 12 h.

MRI post-processing analysis. *T1 mapping*. T1 relaxation times were estimated using the VTR method, before Gd-DTPA injection, with a series of spin-echo images with varying TR and constant TE using the standard saturation recovery equation (1)

$$SI = \rho\left(1 - e^{-\frac{TR}{T1}}\right) \quad (1)$$

where SI is the signal intensity and ρ is the spin density. Nonlinear least-squares fitting is used to fit MRI data to equation (1). The accuracy of the T1 mapping method is a critical step for converting intensity data to concentration versus time curves, as well as selection of the arterial input function (AIF) or brain regions-of-interest, noise filtering, and signal intensity drift correction over the dynamic time course[64,65].

Capillary permeability K_{trans} mapping. We determined the capillary permeability transfer constant, K_{trans}, to intravenously injected gadolinium-based contrast agent in different white matter tracts in mice using a modified method as we reported in humans with the post-processing Patlak analysis[27,64]. We analyzed the following white matter tracts: corpus callosum, internal capsule, cingulum, and external capsule. For comparison, we also analyzed gray matter regions including dorsal hippocampus, posterior thalamus, primary somatosensory barrel cortex, and anterior cingulate cortex. We employed high spatial and temporal resolutions that allowed us to accurately identify the K_{trans} maps in anatomical regions as small as the corpus callosum or cingulum. We determined the AIF in each mouse from the common carotid artery, as previously reported in humans[27]. Individual AIF curves are particularly important for calculating accurately the K_{trans} values if blood flow and volume are influenced by age or a pathological process.

The present Patlak analysis[27,64] requires that the tracer's diffusion (Gd-DTPA) across the capillary vessel wall remains unidirectional during the acquisition time. The total tracer concentration in the tissue, $C_{tissue}(t)$, can be described as a function of the vascular concentration C_{AIF} (t), the intravascular blood volume v_p, and a transfer constant K_{trans} that represents the flow from the intravascular to the extravascular space using equation (2).

$$C_{tissue}(t) = K_{\text{trans}}\int_0^t C_{AIF}(\tau)d\tau + vp \cdot C_{AIF}(t) \quad (2)$$

Post-processing of the collected DCE-MRI data were done using in-house DCE processing software (*Rocketship*) implemented in Matlab[65]. The DCE-MRI test conditions have been developed to calculate the transfer capillary permeability constant K_{trans} for each voxel and each brain region. Data from standard anatomical atlases of the mouse brain were used as guidelines to determine the boundaries of all brain regions on T1-weighted images.

Blood flow assessment. DSC-MRI typically makes use of rapidly acquired MR images after an intravenous bolus injection of a paramagnetic contrast agent[66]. Besides the earlier mentioned T1-shortening effect using DCE techniques, paramagnetic contrast agents such as Gd-DTPA also induce T2*-shortening via magnetic susceptibility effects. The temporary T2*-shortening, caused by passage of MR contrast agent through the microvascular bed, can be measured with a FLASH gradient-echo T2*-weighted MRI sequence.

Following collection of the DSC-MRI data, quantitative post-processing analysis was performed. Analysis routines were written in-house, implemented using Matlab, and described by the equations below. For each voxel, the signal drop after injection depends on the local concentration of contrast agent. We analyzed the following white matter tracts: corpus callosum, internal capsule, cingulum, and external capsule. For comparison, we also analyzed gray matter regions including dorsal hippocampus, posterior thalamus, primary somatosensory barrel cortex, and anterior cingulate cortex. Assuming a linear relationship between signal drop and concentration, these quantities can be related via

$$S(t) = S_0 \times e^{-r_2 * C(t) \times TE} \quad (3)$$

where $S(t)$ is the signal intensity at time t after bolus injection for any given voxel, S_0 is the mean pre-contrast signal intensity, r_2* relaxivity constant of the contrast agent used, $C(t)$ is the concentration of gadolinium as a function of time, and TE is the time echo of the acquisition sequence.

From the previous formula, the conversion from signal to contrast agent concentration is straightforward, and occurs via

$$C(t) = \frac{-1}{r_2 * TE}\ln\left(\frac{s(t)}{s_0}\right) \quad (4)$$

The profile of this concentration curve is heavily influenced by the manner in which the tracer bolus is injected into the mouse. To define the shape of the bolus

© 2018 Nature America, Inc., part of Springer Nature. All rights reserved.

doi:10.1038/nm.4482

curve, a representative AIF was obtained for each mouse individually. The AIF was obtained from the image data via manual delineation, typically from the common carotid arteries (same as for K_{trans} mapping). By defining the residual function, $R(t)$, which represents the fraction of tracer presently circulating at time t, the relationship between tracer concentration and blood flow can be modeled as a convolution between $R(t)$ and the AIF[67]:

$$C_t(t) = \frac{k_H}{\rho} F \int_0^t C_\alpha(\tau) R(t-\tau) d\tau \quad (5)$$

where $C_t(t)$ is the concentration of contrast agent in the tissue, F is parameter that scales $R(t)$ to fit $C_t(t)$, and is proportional to blood flow (BF),, κ_H is the ratio of capillary to artery hematocrit (a value of 0.42 was used), ρ is tissue density (1.04 g/ml), $C_a(t)$ is AIF time course. To solve equation (5), we evoked numerical standard singular value deconvolution approach, as reported[68]. Using this deconvolution, $R(t)$ and F values were obtained, and regional blood flow (BF; ml/100g/min) was computed using the equation

$$BF = \frac{k_H}{\rho} \times F \quad (6)$$

DTI metrics and tractography. To pre-process the raw *ex vivo* DWIs, we first corrected for eddy current distortions using the 'eddy correct' tool in FSL (www.fmrib.ox.ac.uk/fsl). Extra cerebral tissue was removed using the 'skull-stripping' Brain Extraction Tool from BrainSuite (http://brainsuite.org/). All resulting volumes were visually inspected and manually edited as needed. Then, all images were linearly aligned using FSL's 'flirt' function with 12 degrees of freedom to allow for rotation, translation, scaling, and skewing in 3D. The gradient direction tables were rotated accordingly after each linear registration for the 6 diffusion volumes. Furthermore, each skull-stripped b_0 images were elastically registered to a minimum deformation template created using all linearly registered images for both +/+ and F7/F7 mice. This was done to ensure that all scans were in the same space for further analysis.

We applied the DTI model using the FSL's 'dtifit' tool to compute fractional anisotropy (FA), mean diffusivity (MD), axial diffusivity (AD), and radial diffusivity (RD) maps. The diffusion tensor was computed using the eddy corrected and elastically registered DWI scans. A Gaussian low-pass filter with kernel size 3 (that is, 3 × 3 × 3 voxel) was applied to all maps. To test for group differences, a voxel-wise linear regression was run, with F7/F7 mice coded as 1 and +/+ mice coded as 0. We ran this for 4–6-, 12–16- and 36–48-week-old animals separately. A regional false discovery rate (FDR) correction was used to correct for multiple comparisons across voxels. In addition, searchlight-based multivoxel pattern statistics were performed on the resulting probabilistic P value maps from the regression in all cohorts. As we published previously[34], tractography maps were then performed on the eddy corrected DWI scans aligned to the Mori atlas using a deterministic fiber reconstruction method, FACT, in Trackvis (http://trackvis.org/).

Volumetric analysis. Volumetric analyses were performed using trace weighted images (TWI; obtained from *ex vivo* DTI data) and SPM8 software running with Matlab (The MathWorks). The brain regions-of-interest boundaries were manually drawn for each slice using ImageJ. We studied the total white matter (including corpus callosum and external capsule), cortical mantles, and hippocampus volumes in each group of mice including 4–6-, 12–16- and 36–48-week-old age-matched controls (+/+) and pericyte-deficient F7/F7 animals.

Fiber density analysis. To illustrate changes in white matter fiber density, we traced the fiber pathways within each age group in control (+/+) and F7/F7 mice. To do this, we manually created regions-of-interest within the corpus callosum and cingulum using the raw DWI scans to best portray the alterations in the organization of the fibers over time.

Hemosiderin deposits. Hemosiderin deposition was performed using an automatic modified Otsu-thresholding protocol on sagittal T2*-weighted images (see *Ex vivo* T2*-weighted-MRI above). The areas of low intensity that appear on T2*-weighted MRI are larger than the corresponding hemosiderin deposits, representing the so-called 'blooming' effect. This allows the detection of microhemosiderin deposits as small as 5–10 µm. Two white matter regions of interest (that is, corpus callosum and internal capsule), and two gray matter regions (that is, primary somatosensory cortex and hippocampus), were quantified with percentage signal voids (that is, dark voxels containing iron) per brain regions.

Quantitative [^{14}C]iodoantipyrine autoradiography. To measure regional blood flow, we used ^{14}C-iodoantipyrine (^{14}C-IAP) method in combination with blood sampling from the heart as previously reported[17]. In brief, mice were anesthetized with 1.5% isoflurane in 30% oxygen/70% nitrous oxide. Radiolabeled ^{14}C-IAP (20 µCi, American Radiolabeled Chemicals) diluted in 200 µl saline was injected intraperitoneally. Precisely 30 s following ^{14}C-IAP injection, mice were immersed in liquid nitrogen until completely frozen. Frozen blood from the left ventricle of the heart was carefully removed in the cold room (about 0 °C) and placed in pre-weighed microcentrifuge tubes. Blood samples were decolorized with hydrogen peroxide to reduce quenching and dissolved overnight in 1 ml aqueous based tissue solubilizer (SolvableTM, PerkinElmer Life and Analytical Sciences). Following addition of 5 ml high flash-point LSC-cocktail (Ultima GoldTM, PerkinElmer), samples were analyzed for ^{14}C-IAP radioactivity with a liquid scintillation counter (Tri-Carb 2700 TR, Packard Instrument Company). The frozen brains were carefully removed in the cold room and embedded in cold OCT embedding medium on dry ice. Brains were cryosectioned at 20 µm, mounted on glass slides, dried on a hot plate at 55 °C for 10 min and exposed to BioMax MR autoradiographic film (Kodak) along with calibrated autoradiographic ^{14}C standards (GE Healthcare). After 1–4 weeks of exposure, the film was developed and resulting images were analyzed on an MCID imaging analyzer (InterFocus Imaging) to quantitatively determine levels of ^{14}C-IAP in different brain regions. Equation (7) was used to calculate the regional blood flow, BF (ml/100g/min) through different white matter regions as previously described[17]

$$\mathrm{BF} = \frac{\lambda}{\mathrm{T}} \left\{ \frac{\ln[(1 - C_I(T)]}{\lambda \int_0^T C_A(T)} \right\} \quad (7)$$

where $C_I(T)$ is ^{14}C-IAP radioactivity disintegrations per minute (dpm)/g of brain tissue; T is the experimental time in s; $C_A(T)$ is ^{14}C-IAP radioactivity dpm/g plasma determined as ^{14}C-IAP integrated plasma concentration ($_0\int^{\mathrm{T}}$) from ^{14}C-tracer lag time after ^{14}C-IAP intraperitoneal injection (zero time) to the value measured in the frozen blood sample from the heart at the end of the experiment (at time T), by assuming a linear rise or ramp function over T; λ is ^{14}C-IAP central nervous system tissue to blood partition coefficient, 0.8 ml/g. The regional blood flow was calculated with the MCID program.

Viral cortical injections. *Surgery*. Surgical procedures were performed under general anesthesia with isoflurane (1–1.5%) using the SomnoSuite Small Animal Anesthesia System (Kent Scientific). Rectal temperature was monitored and maintained at 36.5 ± 0.5 °C. Heads were shaved to remove hair in a surgical preparation area and bland ophthalmic ointment were placed on the eyes. A midline incision was made above the scalp with a sterile scalpel blade, the underlying periosteum was dissected using blunt dissection techniques, and the skull was cleaned. A small cranial window was opened at coordinates −1.6, −3.2, −0.4 mm (x,y,z) with a 3 mm diameter stainless steel drill under a surgery microscope, leaving the dura intact. Recombinant AAV serotype 2/9 (Penn VectorCore, AV-9-PV2177), viral titer was 2.18 × 10^{13} viral genomes/ml, was withdrawn into a pulled 0.5-mm diameter glass pipette filled with mineral oil. The needle was inserted into the cranial window at the rate of 1 mm/min; 2 min were allowed to elapse for the parenchyma to seal over the needle, then 60 nl of the virus solution was pressure injected at the rate of 12 nl/min via a MicroSyringe Pump controller (World Precision Instruments). 5 min were allowed to elapse for viral diffusion and the needle was withdrawn at the rate of 1 mm/min with a minute pause halfway into withdrawal. Following injection, the wound was cleaned, the cranial window was sealed with bone wax (Lukens), and the skin incision was closed using nylon sutures. Animals were housed for recovery and virus propagation for 21 d before histological analysis.

Quantification. Animals were anesthetized intraperitoneally with 100 mg/kg ketamine and 10 mg/kg xylazine and transcardially perfused with 4% paraformaldehyde (PFA) in 0.01 M phosphate buffer saline (PBS), pH = 7.4, containing 0.005 M EDTA (EDTA). Brains were extracted and post-fixed in 4% PFA overnight. Brains were serially sectioned on a vibratome (Leica VT100S) at 40-µm intervals. Sections were serially mounted and sealed onto slides with 80% PBS,

© 2018 Nature America, Inc., part of Springer Nature. All rights reserved.

20% glycerol and 1:5,000 4′,6-diamidino-2-phenylindole (Dapi) stain medium mix. Sections were imaged (Leica DM600B) at 5× magnification at five regions: primary somatosensory barrel cortex injection site (iS1BF), corpus callosum (CC), ipsilateral dorsal and ventral internal capsule (ICd and ICv, respectively), and contralateral primary somatosensory barrel cortex (cS1BF). Images were taken using consistent parameters across animals. Sequential images were compiled into image stacks for each brain region using ImageJ. Integrated fluorescence density was calculated for each image stack (integrated density of total image – integrated density of background). Results are presented as percentage projection density changes for each brain regions[35]. The integrated density of each region was then normalized to the iS1BF injection site of each individual animal[35].

Behavior. *Complex wheel-running assay*. The complex running wheel test is specific for the mouse corpus callosum injury[69]. Animals were isolated in transfer cages measuring 40 cm by 20 cm with a running wheel measuring 12.5 cm in diameter (Amazon #B0002DGSEC). Animals were trained on the 'regular' wheel with evenly spaced rungs (34 rungs, spaced 1.1 cm apart) for 2 weeks (day 1–14). After the 2-week training period, mice were introduced to the 'complex' wheel with 20 random rungs missing (14 rungs total, 2.2 and 3.3 cm apart). The mice ran spontaneously, without artificial reward, on both regular and complex wheels for the equivalent of 5 to 7 km per night. Number of wheel revolutions was recorded throughout 30-min intervals during the light phase by a Micrologix 1000 programmable controller (Allen-Bradley Cat# 1761-L10BWB F purchased from Royal Wholesale Electric) and measured via a presence/absence laser (Keyence #LR-ZB240CB). Results from each 24 h period were exported to a Microsoft Excel file in which total distance run and maximum velocity were calculated for each mouse: three consecutive 'regular' trials (days 15, 16 and 17), followed by three consecutive 'complex' trials (days 18, 19 and 20). The highest number of revolutions within each day was converted to obtain maximum velocity reached in that day in meters/min[68]. All mice showed spontaneous running activity so that none were excluded on this basis.

Radial arm maze. Specific impairment in spatial working memory on 8-arm radial maze test reflects deficits in the cortico-callosal projections in animals with white matter damage but without hippocampal damage[70]. Prior to testing, mice were subjected to food deprivation (to reduce their initial body weight by 10–15%) since the test performance was dependent on a food reward; the restricted diet was maintained until the end of testing. Mice were pre-trained for 5 min on two consecutive days to familiarize with the experimental environment, maze, food (Fruity Pebbles cereal), and the behavioral task. On pre-training day 1, the cereal was scattered throughout the maze with all 8 doors open and each animal was left to explore freely for 5 min. On pre-training day 2, a single piece of cereal was placed at the end of each arm. The mouse was placed in the central platform and allowed to consume the food in each arm in turn. The doors were automatically controlled.

7 consecutive days of testing began the day after the second pre-training day. The following procedure was performed on each day of testing. A single piece of cereal was placed at the end of each arm. The mouse was placed in the central platform with all arms open and allowed to choose which arm to enter. Once the mouse entered any of the arms, the seven other doors were closed. Upon returning to the central platform from the first arm visit, the arm door closed and the animal was confined to the central platform for 5 s. After the 5 s delay, all arm doors opened and the animal was allowed to make a new choice. The trial ended when the mouse retrieved all 8 pieces of cereal or 25 min had elapsed, whichever occurred first. After each trial, the maze was cleaned with 70% ethanol solution. Trials were recorded with webcam and the number of errors was measured manually by analyzing recorded videos. For each of the 7 trials (performed on 7 consecutive days), we analyzed the number of revisited arms (considered 'errors') and total time to enter all eight arms. The results were analyzed by comparing learning ability of each group on day 1 and day 7.

Novel object recognition. A hippocampus-dependent novel object recognition test (NOR) was performed as we have previously reported with modifications[17,55]. Animals were placed in a 30-cm^3 box and allowed to habituate to the testing area for 10 min. Animals were then placed back in their cages and 2 identical approximately 5 × 5 cm objects were placed in the top left and right corner of the testing area. Animals were allowed to explore the two objects in the testing area for 5 min before being returned to their cages. After 1-h interval, one of the objects was replaced with a new object (different shape and color) and the animals were allowed to explore the testing area once again for 3 min. After each trial, the testing area and the objects was thoroughly cleaned with 70% ethanol solution. All the trials, including habituation, were recorded with a high-resolution camera and the amount of time each animal spent exploring the objects was analyzed. Any animals that presented a preference for either of the two identical objects, before replacement with the novel object/location, were eliminated from the analysis.

Contextual and cued fear conditioning. A hippocampus-dependent fear conditioning tests were performed as previously described[70]. The experiments were performed using standard conditioning chambers housed in a soundproof isolation cubicle and equipped with a stainless-steel grid floor connected to a solid-state shock scrambler. The scrambler was connected to an electronic constant-current shock source that was controlled via an interface connected to a Windows XP computer running FreezeFrame software (Coulbourn Instruments). A digital camera was mounted on the steel ceiling and behavior was monitored. During training, mice were placed in the conditioning chamber for 4 min and received two footshocks (0.25 mA, 2 s) paired with 15-s tone (80 dB) at 1-min interval starting 2 min after placing the mouse in the chamber. The footshock was applied during the last 2 s of the 15-s tone duration. Contextual memory was tested in the same chamber 6 h after the training without footshock or tone applied. Cued memory was tested the next day in the chamber with only the tone applied, and the grid floor was changed to avoid contextual recognition. Hippocampus-dependent fear memory formation was evaluated by scoring freezing behavior (the absence of all movement except for respiration). For the two fear conditioning paradigms, the automated FreezeFrame system was used to score the percentage of total freezing time with a threshold set at 10%.

Nesting. Nest construction test was performed as previously reported[55,69]. 2 h after the beginning of the dark cycle, the animals were individually placed in clean home cages with a single nestlet. Nests were assessed the next morning and evaluated following the five-point scale as we described in detail[69].

Burrowing. Burrowing test was performed as described previously[55]. To assess burrowing behavior, mice were individually placed in cages equipped with a burrow made from a 200-mm-long and 70-mm diameter tube of polyvinyl chloride plastic with one end enclosed. The burrow was filled with 200 g of mouse food pellets, and the mice were allowed to burrow for 2h right before the beginning of the dark cycle. The weight of the remaining food pellets inside the burrow was determined to obtain a measurement of the food amount burrowed.

Gender. We did not find significant gender differences in behavioral tests between males and females within either F7/F7 group and control (+/+) group of mice (distributed approximately in a 1:1 gender ratio in all studied age groups) including the running wheel and radial 8-arm maze tests, hippocampal-dependent tests such as novel object recognition and fear conditioning, and/or activity of daily living tests such as nesting and burrowing. Therefore, for analysis data from both male and female mice were pooled together within each studied age groups of F7/F7 mice and the corresponding age-matched controls.

Electron microscopy. *Electron microscopy procedure*. Animals were sacrificed and transcardially perfused with 2% glutaraldehyde/2% PFA in 0.1 M phosphate buffer (pH = 7.4). Brains were then postfixed for 4 h in the same fixative and were sliced at 50 µm thickness using a Leica vibratome. Sections were postfixed in 2% osmium tetroxide, dehydrated, and flat embedded in 100% Epon between Aclar sheets (Ted Pella). With the use of a stereoscope, parts of the corpus callosum and internal capsule were carefully dissected and placed on Epon blocks. Blocks were coded, and all subsequent procedures were performed blind to genotypes. 70-nm-thick sections were obtained on copper mesh grids using a Reichert ultramicrotome with a diamond knife (Diatome, Biel, Switzerland) and counterstained with 2% uranyl acetate. Ultrastructural analysis was performed using a JEOL JEM-2100 transmission electron microscope. Electron micrographs were captured at x2 – 3K magnifications using a Bio-Scan CCDTV and were saved as high-resolution TIFF files (2048x2048 pixels). Digital images

© 2018 Nature America, Inc., part of Springer Nature. All rights reserved.

doi:10.1038/nm.4482

were optimized for image resolution (final resolution 350 dpi), brightness, and contrast in Photoshop CS6.

Negatively stained fibrin specimens were prepared by floating carbon-coated formvar films mounted on copper grids (EMS) on 10-µl droplets of sample for 5 min. The excess liquid was blotted-off followed by staining with 1% uranyl acetate. Imaging was performed on a JEOL JEM-2100 transmission electron microscope operated at 100 kV.

Quantification. For myelin thickness and axon diameter quantification, electron micrographs from four F7/F7 and four age-matched littermate control (+/+) mice were analyzed. G-ratios were quantified from 300 axons per mouse using ImageJ software and were measured as the axon diameter/total diameter of the axon plus the myelin sheath[71]. Degenerated axons were identified by their lack of myelin and distortion (swelling) of the axoplasm and mitochondria as shown in **Figure 4a** and **Supplementary Figure 10a** with purple stars.

Immunohistochemistry. Mice were anesthetized intraperitoneally with 100 mg/kg ketamine and 10 mg/kg xylazine and transcardially perfused with 20 ml phosphate buffer saline (PBS) containing 0.005 M EDTA followed by 20 ml of 4% PFA. Brains were sectioned at a thickness of 30 µm. Sections were blocked with 5% normal donkey serum (Vector Laboratories)/0.1%Triton-X/0.01 M PBS for 1 h and incubated with primary antibodies diluted in blocking solution overnight at 4 °C. We used the following primary antibodies: for pericyte coverage, polyclonal goat anti-mouse aminopeptidase N/ANPEP (CD13; R&D systems, AF2335; 1:100); for fibrinogen and fibrin extravascular deposits, polyclonal rabbit anti-human fibrinogen (Dako, A0080; 1:500) which recognizes both monomeric form of fibrinogen as well as fibrinogen-derived fibrin polymers and cross reacts with mouse fibrinogen and fibrin[17]; for myelin basic protein (MBP), polyclonal goat anti-human MBP (Santa Cruz, sc-13914-R; 1:500,) which cross reacts with mouse MBP; for axons SMI-312 neurofilament, monoclonal mouse anti-mouse SMI-312 (SMI-312; BioLegend, SMI312; 1:500); for oligodendrocytes, polyclonal rabbit anti-mouse Olig2 (Millipore, AB9610; 1:200) or monoclonal mouse anti-Olig2 (ThermoFisher, MA5-15810; 1:200); for myelinated mature oligodendrocytes, monoclonal mouse anti-cyclic nucleotide phosphodiesterase (CNPase; Abcam, ab6319; 1:500); for oligodendrocyte progenitor cells, monoclonal rabbit anti-platelet-derived growth factor receptor α (PDGFRα; Cell Signaling, #3174; 1:200); for neurons, polyclonal rabbit anti-mouse NeuN (Millipore, ABN78; 1:500); for microglia, rabbit anti-mouse ionized calcium binding adaptor molecule 1 (Iba-1; Wako, 019-19741; 1:1,000); for astrocytes, rabbit anti-glial fibrillary acidic protein (GFAP; Dako, z0334; 1:500). For cultured pericytes, we used a goat anti-human platelet-derived growth factor receptor beta (PDGFRβ; R&D Systems, AF385; 1:100). After incubation in primary antibodies, sections were washed in PBS and incubated with fluorophore-conjugated secondary antibodies (**Supplementary Table 3**), and then mounted onto slides with fluorescence mounting medium (Dako). To visualize brain microvessels, sections were incubated with Dylight 488-conjugated *L. esculentum* lectin (Vector Labs, DL-1174; 1:200) for 1 h. For cellular uptake analysis of exogenous circulating tracers by the white matter tracts, F7/F7 and +/+ littermate controls were assessed by retro-orbital injection of Alexa fluor 555-conjugated Cadaverine (Invitrogen, A30677; 10 µg/g) allowed to circulate for 2 h, as previously described[33]. All images were taken with a Zeiss 510 confocal microscopy and analyzed using ImageJ software (US National Institutes of Health). Gain, digital offset, and laser intensity were kept standardized.

Confocal microscopy analysis. *Lasers and band-pass filters*. We used a 488-nm argon laser to excite Alexa Fluor and Dylight 488, and the emission was collected through a 500–550-nm bp filter; a 543 HeNe laser to excite Alexa Fluor 568 and Cy3 the emission was collected through a 560–615-nm bp filter; a 633 HeNe laser to excite Alexa fluor 649 and the emission was collected through a 650–700-nm bp filter.

Pericyte coverage. The quantification analysis of pericyte coverage and numbers was restricted to CD13-positive perivascular mural cells that were associated with brain capillaries defined as vessels with <6 µm in diameter, as previously described[17,30]. For pericyte coverage, ten-micron maximum projection z-stacks (area 640 × 480 µm) were reconstructed, and the areas occupied by CD13-positive (pericyte) and lectin-positive (endothelium) fluorescent signals on vessels < 6 µm were subjected separately to threshold processing and analyzed using ImageJ. First, black and white 8-bit images for CD13 and lectin signals were thresholded separately using Otsu's thresholding plugin that minimize the intra-class variance of the thresholded black and white pixels. After thresholding, the integrated signal density for each thresholded image was calculated. In order to express the integrated signal density as the area of the image (in pixels) occupied by the fluorescent signal, the integrated signal density was divided by 255 (the maximum pixel intensity for an 8-bit image). The integrated pixel-based area ratios of CD13 and lectin fluorescent signals were used to determine pericyte coverage as a percentage (%) of CD13-positive surface area covering lectin-positive endothelial capillary surface area per field, as previously reported[17]. In each animal, 4-6 randomly selected fields in the corpus callosum (CC), internal capsule (IC) and cingulum (Cing) were analyzed in 4 non-adjacent sections (~100 µm apart), and averaged per mouse.

Pericyte numbers. For pericyte numbers, ten-micron maximum projection z-stacks were reconstructed, and the number of CD13-positive perivascular cell bodies that colocalized with DAPI-positive nuclei on the abluminal side of lectin-positive endothelium on vessels ≤6 µm counted using ImageJ Cell Counter plug-in, as we have previously described[17,30]. In each animal, four to six randomly selected fields (640 × 480 µm) in the corpus callosum were analyzed in four non-adjacent sections (~100 µm apart), and averaged per mouse. The number of pericytes was expressed per mm2 of tissue.

Extravascular fibrinogen and fibrin deposits. For quantification of extravascular fibrinogen and fibrin deposits with an antibody that detects both monomeric fibrinogen and fibrinogen-derived fibrin polymers. 10-µm maximum projection z-stacks were reconstructed, and the fibrinogen and fibrin-positive perivascular signal on the abluminal side of lectin-positive endothelial profiles on microvessels ≤6 µm in diameter was subjected to threshold processing and analyzed using ImageJ[17]. In each animal, four to six randomly selected fields in the corpus callosum, internal capsule, and cingulum were analyzed in four non-adjacent sections (~100 µm apart).

MBP-positive myelin. Ten microns maximum projection z-stacks were reconstructed, and MBP-positive signal was subjected to threshold processing and was analyzed using ImageJ. In each animal, four to six randomly selected fields in the corpus callosum and internal capsule were analyzed in four non-adjacent sections (~100 µm apart).

SMI-312-positive axons. As previously described[17], 10-µm maximum projection z-stacks were reconstructed, and SMI-312-positive signal was subjected to threshold processing and was analyzed using ImageJ. In each animal, four to six randomly selected fields in the corpus callosum and internal capsule were analyzed in four non-adjacent sections (~100 µm apart).

Enlarged perivascular spaces. Brain sections were stained with MBP and endothelial lectin. 10-µm maximum projection z-stacks were reconstructed, and the perivascular space between lectin-positive endothelial microvessel profiles and MBP-positive myelin were manually determined using ImageJ. As reported with modifications[17], EPVS was defined as a perivascular space over 3 µm, and was quantified in the corpus callosum and external capsule regions, and expressed as the number of vessels with EPVS per mm^2.

NeuN-positive neuron counts. Ten microns maximum projection z-stacks were reconstructed, and the number of NeuN-positive neurons per mm^2 was determined as previously described using the ImageJ Software Cell Counter plugin analysis tool[18]. In each animal, four to six randomly selected fields (420 × 420 µm) from primary somatosensory barrel cortex (layer IV-V) and dorsal hippocampus (CA1 subfield) were analyzed in four non-adjacent sections (~100 µm apart).

Oligodendrocytes counts. 10-µm maximum projection z-stacks were reconstructed, and the number of oligodendrocytes (Olig2-positive cells), myelinated mature oligodendrocytes (CNPase-positive cells), oligodendrocytes progenitor cells (PDGFRα-positive cells), as well as oligodendrocytes death (TUNEL- and Olig2-double positive cells) in the corpus callosum and internal capsule per mm^2 were determined as previously described using the ImageJ Software cell counter plugin analysis tool. In each animal, four to six randomly selected fields (420 × 420 µm) from corpus callosum and internal capsule were analyzed in four non-adjacent sections (~100 µm apart).

© 2018 Nature America, Inc., part of Springer Nature. All rights reserved.

Cell death assays. For quantification of cell death, terminal deoxynucleotidyl transferase dUTP nick end labeling (TUNEL) assay was performed following the manufacturer's instructions (Roche) and as we previously reported[17].

Hypoxyprobe-1 tissue staining and analysis. For determination of hypoxic tissue mice were injected intraperitoneally with 60 mg/kg hypoxyprobe-1 pimonidazole (Hypoxyprobe-1™) 4 h before harvesting brains for tissue processing and staining according to the manufacturer's instructions. 10-µm maximum projection z-stacks were reconstructed, and hypoxic area of the hypoxyprobe-1 positive signal obtained from the cortex and hippocampus was quantified using ImageJ, as we previously reported[17].

Microvascular density. 10-µm maximum projection z-stacks were reconstructed, and the length of lectin-positive microvasculature profiles was measured using the ImageJ plugin 'Neuro J' length analysis tool from 3-6 randomly selected fields in the corpus callosum, internal capsule, primary somatosensory barrel cortex, and dorsal hippocampus (420 × 420 µm) per section from four non-adjacent (~100 µm apart) sections per animal, as we described[17]. The length was expressed in millimeters of lectin-positive vascular profiles per mm^3 of brain tissue.

Microglia and astrocytes counts. Ten microns maximum projection z-stacks were reconstructed, and the number of Iba-1-positive microglia and GFAP-positive astrocytes per mm^2 were determined using the ImageJ Software Cell Counter plugin analysis tool, as we previously described[17]. In each animal, four to six randomly selected fields (420 × 420 µm) from corpus callosum were analyzed in four non-adjacent sections (~100 µm apart). In a separate experiment, we performed immunostaining for microglia (Iba-1) and fibrin(ogen), and astrocytes (GFAP) and fibrin(ogen), and determined the numbers of microglia and astrocytes at sites with no fibrin deposition compared to sites with a different degree of fibrin deposition at early (4–6 weeks of age) and later (36–48 weeks of age) time points in F7/F7 mice. In each mouse, 50 randomly selected 50 × 50 µm-sized boxes in areas with and without fibrin(ogen) deposition derived from six adjacent tissue sections 100 µm apart was taken for analysis. For each age group, 150 individual points per group in areas with and without fibrin(ogen) deposition were analyzed from three mice per group.

Bright-field microscopy analysis. *Luxol fast blue staining*. Animals were anesthetized and perfused as described above and brains were immersed in 4% PFA overnight. Brains were paraffin embedded, and sectioned on a microtome (Leica RM2125) at 6-µm intervals. Sections were mounted on slides, air-dried and stained with Luxol Fast Blue/CE Violet Kit (Americanmastertech, Catalog: KTLFB) according to the manufacturer's instructions. Slides were covered and sealed with Cytoseal 60 (American MasterTech). Sections were imaged under a light microscope (Keyence BZ-9000). Severity of white matter damage was graded, following the Fazekas scale[72] in the medial corpus callosum as normal (grade 0); disarrangement of nerve fibers (grade 1); formation of marked vacuoles (grade 2); and the disappearance of myelinated fibers (grade 3).

Hematoxylin staining. Animals were anesthetized and perfused as described above and brains were immersed in 4% PFA overnight. Brains were paraffin embedded, and sectioned on a microtome (Leica RM2125) at 6-µm intervals. Brain sections were then rehydrated and stained with FD Hematoxylin solution according to the manufacturer's instructions (FD Neurotechnologies). Representative images were taken in the primary somatosensory barrel cortex (S1Cx) and CA1 hippocampal subfield in coronal sections at 2 mm posterior to the Bregma.

Flow cytometry. Animals were transcardially perfused with 0.01 M PBS and brains immediately removed. White matter tissue (corpus callosum, internal capsule, cingulum, and external capsule) was isolated from the brains, trypsinized for 30 min in 0.25% trypsin at 37 °C and then further dissociated using a glass homogenizer. Cells were fixed in 4% PFA for 10 min, blocked in 10% NDS/0.1% Triton-X/1X PBS, stained with mature oligodendrocyte markers rabbit proteolipid protein (PLP; Abcam, ab105784; 1:2,000) and mouse MBP (SMI-99; BioLegend; 1:500), followed by incubation in secondary 488- (Invitrogen; 1:200) and 647-Alexa Fluor (Invitrogen; 1:200) respectively. Cells were then sorted using BD SORP FACSAria I (Becton-Dickinson). Control stains (unstained and MBP- or PLP- single stained cells) were used to set gates. All samples were then FSC-A and SSC-A gated, followed by FSC-A/FSC-H gating to select singlet cells. Subsequent relevant gating was conducted. Ten thousand events were originally collected from which positively-gated cells showed 95–98% purity. Data was acquired with FACSDiva 8.0.1 software and analyzed with FlowJo V10 for quantification of mature oligodendrocytes.

Immunoblotting. White matter tissue (that is, corpus callosum, internal capsule, cingulum, and external capsule) was lysed in RIPA buffer (50 mM Tris, pH 8.0, 150 mM NaCl, 0.1% Sodium Dodecyl Sulfate (SDS), 1.0% NP-40, 0.5% sodium deoxycholate and Roche protease inhibitor cocktail). Samples were then subjected to bis-tris-SDS-PolyAcrylamide Gel Electrophoresis (SDS-PAGE) and transferred to a nitrocellulose membrane. Membranes were blocked with 5% milk, incubated with anti-MBP (Santa Cruz, sc-13914; 1:1,000), and then incubated with HRP-conjugated donkey anti-goat secondary antibody (Invitrogen, A16005; 1:5,000). Membranes were then treated with Immobilon Western ECL detection buffers (Millipore), exposed to CL-XPosure film (Thermo Scientific) and developed in a X-OMAT 3000 RA film processor (Kodak).

Cytokine and chemokine expression. In addition to quantifying Iba1-positive microglia and GFAP-positive astrocytes, we analyzed relative abundance of several neuroinflammatory cytokines and chemokines (that is, tumor necrosis factor alpha (*Tnf-α*), interleukin 6 (*Il-6*), interleukin 1 beta (*Il-1β*), chemokine C-C motif ligand 2 (*Ccl2*), and intercellular adhesion molecule 1 (*Icam-1*)) through quantitative real-time polymerase chain reaction using ribonucleic acid (RNA) isolated from snap-frozen brain samples as we previously described[17]. Gene expression was normalized to the house-keeping gene 18S ribosomal RNA (rRNA). All primers are listed in **Supplementary Table 4**.

Cell cultures. *Mouse oligodendrocytes*. A2B5-positive oligodendrocyte precursor cells (OPCs) were isolated from cortices of 129S1/Svlmj P3-P6 mouse pups by magnetic cell sorting (MACS, Miltenyi Biotec), as previously described[73]. Briefly, brains were removed, minced, and further processed using Neural Dissociation Kit following the manufacturer's instructions (#130-092-628, Miltenyi Biotec). Tissue was first digested in warm solution of enzyme P, reaction was quenched with enzyme A buffer and tissue was manually dissociated using three fire-polished Pasteur pipettes with decreasing diameter. Cells were then filtered, centrifuged and resuspended in Dulbecco's Modified Eagle Medium (DMEM) (Invitrogen) containing 1% fetal bovine serum (FBS) (Hyclone), placed in blocking reagent followed by magnetic labeling using anti-A2B5 microbeads (#130-093-392, Miltenyi Biotec), and washed and magnetically sorted using MACS LS columns (#130-042-401, Miltenyi Biotec). OPCs were plated at a density of 5×10^4 cells on poly-D-lysine (PDL)-coated coverslips for cell viability and immunocytochemistry experiments or on PDL-coated six-well dishes for western blotting and caspase-3 activity assays. OPCs were allowed to differentiate into mature oligodendrocytes in medium containing DMEM-SATO based growth medium+Forskolin+NT3+T3 (T3 is the active hormone, 3,5,30-tri-iodothyronine), which has been shown to promote oligodendrocyte differentiation from OPCs[73,74]. Experiments were performed on 7 d *in vitro* mature oligodendrocyte cultures that were approximately 90% positive for myelin basic protein (MBP, a marker of mature oligodendrocytes)[74], and negative for O4, a marker for an intermediate transitional cell type (pre-immature oligodendrocytes) between OPCs and mature oligodendrocytes. Oligodendrocytes were arborized in shape[74]. The cultures did not contain astrocytes (negative for GFAP) or microglia (negative for Iba-1). Mature oligodendrocytes were exposed to either hypoxic conditions (oxygen and glucose deprivation)[75] or treated with soluble fibrinogen or fibrin, as described below.

Mouse pericytes. Brain microvascular pericytes were purchased from ScienCell (#M1200). Cells were cultured in mouse pericyte medium (#1231, ScienCell) in 5% CO_2 at 37 °C. Pericyte cultures were positive for pericyte markers PDGFRβ, NG2 and CD13, and negative for GFAP (astrocytes), CD31 (endothelial cells) and CD11b (microglia). Early passage (P2–3) cultures were used in the study.

Oxygen and glucose deprivation. For OGD experiment, oligodendrocytes were cultured in DMEM without glucose (Invitrogen) in a humidified incubator chamber (Billups-Rothenberg) with 1% O_2 at 37 °C for 6 h, as previously described[75]. After 6 h, cells were removed from the chamber and processed for immunocytochemistry. Pericyte cultures were subjected to OGD as described above at 70% confluence.

© 2018 Nature America, Inc., part of Springer Nature. All rights reserved.

doi:10.1038/nm.4482

Fibrinogen and fibrin treatment. In all studies, we used highly purified fibrinogen that was plasminogen-depleted and >95% clottable (Cat. # 341578, EMD Millipore, Sigma). Fibrinogen (0.25, 0.5, 1 and 1.5 mg/ml) was added to mouse mature oligodendrocyte cultures, 70% confluent pericyte cultures or 70% confluent astrocyte cultures followed by the addition of 4 U/ml hirudin (Cat. # 377853-2000U, Calbiochem). To generate fibrin, fibrinogen (0.01, 0.025 and 0.1 mg/ml) was added to Eppendorf tubes containing oligodendrocyte or pericyte culture media with 1.8 mM $CaCl_2$. To convert fibrinogen to fibrin, we added 0.1 U/ml of thrombin (T-4393, Sigma) for 60 min. Thrombin activity was inhibited by hirudin (4 U/ml). The formation of fibrin polymers has been demonstrated by 4–12% bis-tris-SDS-PAGE followed by silver staining showing cross-linked fibrinogen γ-chains, and transmission electron microscopy showing fibrin polymers (fibrils) ranging from 200 nm to 2 μm in size[76]. We did not see fibrin fibrils crisscrossing and forming a mesh. Cultured medium containing fibrin polymers was added to oligodendrocyte or pericyte cultures. In a separate experiment, inactivated thrombin (thrombin + hirudin) was added to cell cultures as an independent control.

Immunocytochemistry. After OGD (hypoxia), mature oligodendrocytes were detected with an anti-mouse myelin basic protein (MBP) monoclonal antibody (SMI-99; Covance; 1:500), and pericytes with a goat anti-mouse PDGFRβ polyclonal antibody (R&D Systems, #AF1042; 1:500), followed by TUNEL and Dapi-Fluoromount-G (SouthernBiotech) staining. Secondary antibodies were donkey anti-mouse Alexa Fluor IgG 568 (Invitrogen; 1:500) for MBP-positive oligodendrocytes, and anti-goat Alexa Fluor IgG 568 (Invitrogen; 1:500) for PDGFRβ-positive pericytes. TUNEL assay (Roche) was performed after SMI-99 or PDGFRβ immunostaining. Oligodendrocyte and pericyte cell death after OGD was expressed as the percentage of TUNEL-positive cells of MBP-positive oligodendrocytes or PDGFRβ-positive pericytes, respectively.

Double immunostaining for fibrin(ogen) (rabbit anti-human polyclonal antibody cross reacts with mouse fibrinogen, DAKO, #A0080; 1:500) and MBP (as above) was performed to determine fibrin(ogen) accumulation in oligodendrocytes. Secondary antibodies were donkey anti-mouse Alexa Fluor IgG 568 (Invitrogen; 1:500) for MBP-positive cells and donkey anti-rabbit Alexa Fluor IgG 488 (Invitrogen; 1:500) for fibrinogen. To verify intracellular uptake of fibrin(ogen) by mature oligodendrocytes, orthogonal projection views of MBP+/Fibrin(ogen)+ cells were created from fifteen-micron maximum projection intensity z-stacks using ImageJ.

Triple staining with CytoID Autophagy Kit (ENZO Life Sciences, ENZ-51031-K200) on live cells followed by immunostaining for the active form of caspase 3 (rabbit anti-mouse polyclonal, Abcam, ab13847; 1:250) and MPB or PDGFRβ (as above) was done to visualize the formation of autophagosomes and activation of caspase 3 in oligodendrocyte and pericyte cultures, respectively, at different time points. Secondary antibody for active caspase 3 was donkey anti-rabbit 647 Alexa Fluor (Invitrogen; 1:500); secondary antibodies for MBP-positive oligodendrocytes and PDGFRβ-positive pericytes were as described above. In some experiments, the autophagy inhibitors, mTOR activator MHY1485 (Calbiochem, # 500554, 2 μM)[52] and autophagy inhibitor VII (Calbiochem, # 534360, 100 μM)[53] were added to the culture media simultaneously with fibrin(ogen).

To access availability of oxygen to cultured oligodendrocytes in the presence of fibrin (0.1 mg/ml; that is, the highest concentration used to treat cells), we employed Image-iT Hypoxia Reagent for live cells (5 μM, ThermoFisher, H10498), and determined whether fibrin can interfere with oxygen delivery to cells making them hypoxic. We also used Alexa 594-conjugated transferrin (25 μg/ml; ThermoFisher, T13343) to determine whether fibrin (0.01 and 0.1 mg/ml) or fibrinogen (1.5 mg/ml) interfere with uptake of transferrin from the culture medium by plated oligodendrocytes. Transferrin was added for 20 min at indicated time points.

Live/dead assays. Mature oligodendrocytes and pericytes were treated with different concentrations of fibrinogen (0.25–1.5 mg/ml), fibrin (0.01–0.1 mg/ml), ancrod (0.004 IU/ml) as previously reported[77], or TXA (640 μM), as previously reported[78], and cell viability was determined by live/dead assay (ThermoFisher, L3224), as per manufacturer's instructions.

Immunoblotting. The autophagy markers were analyzed in oligodendrocytes 12 and 24 h after treatment with 1.5 mg/ml fibrinogen or 0.1 mg/ml fibrin, with or without mTOR activator MHY1485 (#500554, Calbiochem) or autophagy inhibitor VII (#534360, Calbiochem). Cells were lysed in RIPA buffer (50 mM Tris, pH 8.0, 150 mM NaCl, 0.1% SDS, 1.0% NP-40, 0.5% sodium deoxycholate and Roche protease inhibitor cocktail). Samples were then subjected to NuPAGE 4–12% bis-tris-SDS-PAGE (ThermoFisher) and transferred to a nitrocellulose membrane. Membranes were blocked with SuperBlock (ThermoFisher), incubated with anti-p62 (Cell Signaling, #5114; 1:1,000) or anti-LC3 (Cell Signaling, #4108; 1:1,000) rabbit polyclonal antibodies, and then incubated with HRP-conjugated donkey anti-rabbit secondary antibody (ThermoFisher, #A16023; 1:5,000). Membranes were then treated with SuperSignal West Pico PLUS chemiluminescent substrate (#34580, ThermoFisher), exposed to CL-XPosure film (#34097, Thermo Scientific) and developed in a X-OMAT 3000 RA film processor (Kodak). Relative abundance of the LC3-II/I ratio was quantified against the loading control β-actin as described[79].

Caspase 3 activity. Caspase 3 activity was measured 12 and 24 h after treatment of oligodendrocytes with 1.5 mg/ml fibrinogen or 0.1 mg/ml fibrin, with or without mTOR activator MHY1485 (#500554, Calbiochem) or autophagy inhibitor VII (#534360, Calbiochem). Cells were washed three times with phosphate-buffered saline and the activity assay was performed as per manufacturer's instructions (ApoAlert caspase-3 fluorescent assay kit #630215, Clontech), as we previously reported[80].

Statistical analysis. Sample sizes were calculated using nQUERY assuming a two-sided alpha-level of 0.05, 80% power, and homogeneous variances for the two samples to be compared, with the means and common s.d. for different parameters predicted from published data and our previous studies. The K_{trans} constant and blood flow measurements from the pilot experiments indicated that the sample sizes from 5–7 are sufficient to detect a significant effect ≥ 20% between the studied groups. Our actual sample sizes for both *in vivo* and *ex vivo* MRI parametric maps were 5–7. For comparison between two groups, F test was conducted to determine the similarity in the variances between the groups that are statistically compared, and statistical significance was analyzed by Student's *t* test. Lilliefors test was used to test normality of the data (XLSTAT). For multiple comparisons, the F test was also used to determine the equality of variances between the groups compared and one-way analysis of variance (ANOVA) followed by Bonferroni's post hoc test was used to test statistical significance between control and mutant mice as well as to test for age-related differences within the mutant group. All analyses were performed using GraphPad Prism 7.04v software and by an investigator blinded to the experimental conditions. Data are presented as mean ± s.d., or mean ± s.e.m. as indicated in the figure legends. A P value > 0.05 was considered statistically non-significant.

Life Sciences Reporting Summary. Further information on experimental design is available in the **Life Sciences Reporting Summary**.

Data availability. The data that support the findings of this study are available from the corresponding author upon reasonable request. Uncropped western blots are available in **Supplementary Figure 17**.

61. Zhao, Z. *et al*. Central role for PICALM in amyloid-β blood-brain barrier transcytosis and clearance. *Nat. Neurosci*. **18**, 978–987 (2015).
62. Basham, M.E. & Seeds, N.W. Plasminogen expression in the neonatal and adult mouse brain. *J. Neurochem*. **77**, 318–325 (2001).
63. Ma, Q. *et al*. NLRP3 inflammasome contributes to inflammation after intracerebral hemorrhage. *Ann. Neurol*. **75**, 209–219 (2014).
64. Barnes, S.R. *et al*. Optimal acquisition and modeling parameters for accurate assessment of low Ktrans blood-brain barrier permeability using dynamic contrast-enhanced MRI. *Magn. Reson. Med*. 10.1002/mrm.25793 (2015).
65. Barnes, S.R. *et al*. ROCKETSHIP: a flexible and modular software tool for the planning, processing and analysis of dynamic MRI studies. *BMC Med. Imaging* **15**, 19 (2015).
66. Muir, E.R. *et al*. Quantitative cerebral blood flow measurements using MRI. *Methods Mol. Biol*. **1135**, 205–211 (2014).
67. Ostergaard, L., Weisskoff, R.M., Chesler, D.A., Gyldensted, C. & Rosen, B.R. High resolution measurement of cerebral blood flow using intravascular tracer bolus passages. Part I: Mathematical approach and statistical analysis. *Magn. Reson. Med*. **36**, 715–725 (1996).

© 2018 Nature America, Inc., part of Springer Nature. All rights reserved.

68. Schalomon, P.M. & Wahlsten, D. Wheel running behavior is impaired by both surgical section and genetic absence of the mouse corpus callosum. *Brain Res. Bull.* **57**, 27–33 (2002).
69. Winkler, E.A. *et al.* GLUT1 reductions exacerbate Alzheimer's disease vasculo-neuronal dysfunction and degeneration. *Nat. Neurosci.* **18**, 521–530 (2015).
70. Shibata, M. *et al.* Selective impairment of working memory in a mouse model of chronic cerebral hypoperfusion. *Stroke J. Cereb. Circ.* **38**, 2826–2832 (2007).
71. Fyffe-Maricich, S.L., Schott, A., Karl, M., Krasno, J. & Miller, R.H. Signaling through ERK1/2 controls myelin thickness during myelin repair in the adult central nervous system. *J. Neurosci. Off. J. Soc. Neurosci.* **33**, 18402–18408 (2013).
72. Fazekas, F. *et al.* Pathologic correlates of incidental MRI white matter signal hyperintensities. *Neurology* **43**, 1683–1689 (1993).
73. Cizkova, D. *et al.* Enrichment of rat oligodendrocyte progenitor cells by magnetic cell sorting. *J. Neurosci. Methods* **184**, 88–94 (2009).
74. Zuchero, J.B. *et al.* CNS myelin wrapping is driven by actin disassembly. *Dev. Cell* **34**, 152–167 (2015).
75. Zhu, H. *et al.* Effect of hypoxia/reoxygenation on cell viability and expression and secretion of neurotrophic factors (NTFs) in primary cultured schwann cells. *Anat. Rec. (Hoboken)* **2007**, 865–870 (2010).
76. Gorkun, O.V., Veklich, Y.I., Weisel, J.W. & Lord, S.T. The conversion of fibrinogen to fibrin: recombinant fibrinogen typifies plasma fibrinogen. *Blood* **89**, 4407–4414 (1997).
77. Liu, S. *et al.* Ancrod and fibrin formation: perspectives on mechanisms of action. *Stroke* **42**, 3277–3280 (2011).
78. Lu, Z., Korotcova, L., Murata, A., Ishibashi, N. & Jonas, R.A. Aprotinin, but not ε-aminocaproic acid and tranexamic acid, exerts neuroprotection against excitotoxic injury in an in vitro neuronal cell culture model. *J. Thorac. Cardiovasc. Surg.* **147**, 1939–1945 (2014).
79. Liang, Q. *et al.* Zika Virus NS4A and NS4B Proteins Deregulate Akt-mTOR Signaling in Human Fetal Neural Stem Cells to Inhibit Neurogenesis and Induce Autophagy. *Cell Stem Cell* **19**, 663–671 (2016).
80. Guo, H. *et al.* Neuroprotective activities of activated protein C mutant with reduced anticoagulant activity. *Eur. J. Neurosci.* **29**, 1119–1130 (2009).

© 2018 Nature America, Inc., part of Springer Nature. All rights reserved.

doi:10.1038/nm.4482

nature research

Corresponding author(s): Berislav V. Zlokovic

Life Sciences Reporting Summary

Nature Research wishes to improve the reproducibility of the work that we publish. This form is intended for publication with all accepted life science papers and provides structure for consistency and transparency in reporting. Every life science submission will use this form; some list items might not apply to an individual manuscript, but all fields must be completed for clarity.

For further information on the points included in this form, see Reporting Life Sciences Research. For further information on Nature Research policies, including our data availability policy, see Authors & Referees and the Editorial Policy Checklist.

Please do not complete any field with "not applicable" or n/a. Refer to the help text for what text to use if an item is not relevant to your study.
For final submission: please carefully check your responses for accuracy; you will not be able to make changes later.

Experimental design

1. Sample size

Describe how sample size was determined.

Online Methods, 'Statistical Analysis' section: "Sample sizes were calculated using nQUERY assuming a two-sided alpha-level of 0.05, 80% power, and homogeneous variances for the 2 samples to be compared, with the means and common standard deviation for different parameters predicted from published data and our previous studies."

2. Data exclusions

Describe any data exclusions.

Online Methods, Animals section: "Because previous studies in mice with deficient PDGFRβ signaling did not find the effect of gender on pericyte coverage, BBB integrity or blood flow regulation, both male and female mice at 2, 4-6, 12-16, and 36-48 weeks of age were used in the study... All animals were randomized for their genotype information and were included in the study."

3. Replication

Describe the measures taken to verify the reproducibility of the experimental findings.

For each series of experiments, all replication attempts were successful.

4. Randomization

Describe how samples/organisms/participants were allocated into experimental groups.

Online Methods, 'Animals' section: "All animals were randomized for their genotype information and were included in the study."

5. Blinding

Describe whether the investigators were blinded to group allocation during data collection and/or analysis.

Online Methods, 'Animals' section: "The operators responsible for experimental procedure and data analysis were blinded and unaware of group allocation throughout the experiments." and 'Statistical Analysis' section: "All analyses were performed using GraphPad Prism 7.04v software and by an investigator blinded to the experimental conditions."

Note: all in vivo studies must report how sample size was determined and whether blinding and randomization were used.

Nature Medicine: doi:10.1038/nm.4482

6. Statistical parameters

For all figures and tables that use statistical methods, confirm that the following items are present in relevant figure legends (or in the Methods section if additional space is needed).

n/a	Confirmed	
☐	☒	The exact sample size (*n*) for each experimental group/condition, given as a discrete number and unit of measurement (animals, litters, cultures, etc.)
☐	☒	A description of how samples were collected, noting whether measurements were taken from distinct samples or whether the same sample was measured repeatedly
☐	☒	A statement indicating how many times each experiment was replicated
☐	☒	The statistical test(s) used and whether they are one- or two-sided *Only common tests should be described solely by name; describe more complex techniques in the Methods section.*
☐	☒	A description of any assumptions or corrections, such as an adjustment for multiple comparisons
☐	☒	Test values indicating whether an effect is present *Provide confidence intervals or give results of significance tests (e.g. P values) as exact values whenever appropriate and with effect sizes noted.*
☐	☒	A clear description of statistics including central tendency (e.g. median, mean) and variation (e.g. standard deviation, interquartile range)
☐	☒	Clearly defined error bars in all relevant figure captions (with explicit mention of central tendency and variation)

See the web collection on statistics for biologists for further resources and guidance.

Software

Policy information about availability of computer code

7. Software

Describe the software used to analyze the data in this study.

Matlab R2013a was used for MRI analyses. For DCE-MRI datasets, we used our GUI code running with Matlab (https://github.com/petmri/ROCKETSHIP). We also used statistical parametric mapping SMP8 running with Matlab too for volumetric studies and ROI identifications. We used FreezeFrame software for fear conditioning behavioral analysis. Flow cytometry data were acquired with FACSDiva 8.0.1 software and analyzed with FlowJo V10. ImageJ 1.48v was also used for MRI and histology image processing. Finally, GraphPad Prism 7.04v was used to analyze the data.

For manuscripts utilizing custom algorithms or software that are central to the paper but not yet described in the published literature, software must be made available to editors and reviewers upon request. We strongly encourage code deposition in a community repository (e.g. GitHub). *Nature Methods* guidance for providing algorithms and software for publication provides further information on this topic.

Materials and reagents

Policy information about availability of materials

8. Materials availability

Indicate whether there are restrictions on availability of unique materials or if these materials are only available for distribution by a third party.

No unique materials were used.

Nature Medicine: doi:10.1038/nm.4482

9. Antibodies

Describe the antibodies used and how they were validated for use in the system under study (i.e. assay and species).

For immunofluorescence analysis in human tissue samples, we used the following antibodies: for pericyte coverage - polyclonal goat anti-human PDGFRβ (R&D systems, AF385; 1:100), for fibrinogen and fibrin extravascular deposits - polyclonal rabbit anti-human fibrinogen (Dako, A0080; 1:500), and species-specific fluorochrome-conjugated secondary antibodies were incubated for 1 h at room temperature.

We used the following antibodies in mouse tissue samples: for pericyte coverage - polyclonal goat anti-mouse aminopeptidase N/ANPEP (CD13; R&D systems, AF2335; 1:100); for fibrinogen and fibrin extravascular deposits - polyclonal rabbit anti-human fibrinogen (Dako, A0080; 1:500) which recognizes both monomeric form of fibrinogen as well as fibrinogen-derived fibrin polymers and cross reacts with mouse fibrinogen and fibrin17; for myelin basic protein (MBP) - polyclonal goat anti-human MBP (Santa Cruz, sc-13914-R; 1:500,) which cross reacts with mouse MBP; for axons SMI-312 neurofilament - monoclonal mouse anti-mouse SMI-312 (SMI-312; BioLegend, SMI312; 1:500); for oligodendrocytes - polyclonal rabbit anti-mouse Olig2 (Millipore, AB9610; 1:200) or monoclonal mouse anti-Olig2 (ThermoFisher, MA5-15810; 1:200); for myelinated mature oligodendrocytes - monoclonal mouse anti-cyclic nucleotide phosphodiesterase (CNPase; Abcam, ab6319; 1:500); for oligodendrocyte progenitor cells - monoclonal rabbit anti-platelet-derived growth factor receptor α (PDGFRα; Cell Signaling, #3174; 1:200); for neurons - polyclonal rabbit anti-mouse NeuN (Millipore, ABN78; 1:500); for microglia - rabbit anti-mouse ionized calcium binding adaptor molecule 1 (Iba-1; Wako, 019-19741; 1:1,000); for astrocytes - rabbit anti-Glial Fibrillary Acidic Protein (GFAP; Dako, z0334; 1:500). For cultured pericytes, we used a goat anti-human platelet-derived growth factor receptor beta (PDGFRβ; R&D Systems, AF385; 1:100). After incubation in primary antibodies, sections were washed in PBS and incubated with fluorophore-conjugated secondary antibodies, and then mounted onto slides with fluorescence mounting medium (Dako).

We used the following antibodies in vitro: after OGD, mature oligodendrocytes were detected with an anti-mouse myelin basic protein (MBP) monoclonal antibody (SMI-99; Covance; 1:500), and pericytes with a goat anti-mouse PDGFRβ polyclonal antibody (R&D Systems, #AF1042; 1:500), followed by TUNEL and Dapi-Fluoromount-G (SouthernBiotech) staining. Secondary antibodies were donkey anti-mouse Alexa Fluor IgG 568 (Invitrogen; 1:500) for MBP-positive oligodendrocytes, and anti-goat Alexa Fluor IgG 568 (Invitrogen; 1:500) for PDGFRβ-positive pericytes. TUNEL assay (Roche) was performed after SMI-99 or PDGFRβ immunostaining.
Double immunostaining for fibrin(ogen) (rabbit anti-human polyclonal antibody cross reacts with mouse fibrinogen, DAKO, #A0080; 1:500) and MBP (as above) was performed to determine fibrin(ogen) accumulation in oligodendrocytes. Secondary antibodies were donkey anti-mouse Alexa Fluor IgG 568 (Invitrogen; 1:500) for MBP-positive cells and donkey anti-rabbit Alexa Fluor IgG 488 (Invitrogen; 1:500) for fibrinogen.
Triple staining with CytoID Autophagy Kit (ENZO Life Sciences, ENZ-51031-K200) on live cells followed by immunostaining for the active form of caspase 3 (rabbit anti-mouse polyclonal, Abcam, ab13847; 1:250) and MPB or PDGFRβ (as above) was done to visualize the formation of autophagosomes and activation of caspase 3 in oligodendrocyte and pericyte cultures, respectively, at different time points. Secondary antibody for active caspase 3 was donkey anti-rabbit 647 Alexa Fluor (Invitrogen; 1:500); secondary antibodies for MBP-positive oligodendrocytes and PDGFRβ-positive pericytes were as described above.
To access availability of oxygen to cultured oligodendrocytes in the presence of fibrin (0.1 mg/mL; i.e., the highest concentration used to treat cells), we employed Image-iT Hypoxia Reagent for live cells (5 µM, ThermoFisher, H10498), and determined whether fibrin can interfere with oxygen delivery to cells making them hypoxic. We also used Alexa 594-conjugated transferrin (25 µg/mL; ThermoFisher, T13343) to determine whether fibrin (0.01 and 0.1 mg/mL) or fibrinogen (1.5 mg/mL) interfere with uptake of transferrin from the culture medium by plated oligodendrocytes.

All details were provided within the Online Methods, 'Human Postmortem Studies - Histopathological Analyses', 'Immunohistochemistry', and 'Cell Cultures - Immunocytochemistry' sections, also including two summary tables of all antibodies (for both human and mouse analyses), dilutions, species, potential cross-reactions, catalog numbers, manufactures, and citations when possible.

10. Eukaryotic cell lines

a. State the source of each eukaryotic cell line used.

No eukaryotic cell lines were used.

b. Describe the method of cell line authentication used.

No eukaryotic cell lines were used.

c. Report whether the cell lines were tested for mycoplasma contamination.

No eukaryotic cell lines were used.

d. If any of the cell lines used are listed in the database of commonly misidentified cell lines maintained by ICLAC, provide a scientific rationale for their use.

No commonly misidentified cell lines were used.

Nature Medicine: doi:10.1038/nm.4482

Animals and human research participants

Policy information about studies involving animals; when reporting animal research, follow the ARRIVE guidelines

11. Description of research animals

Provide all relevant details on animals and/or animal-derived materials used in the study.

Platelet-derived growth factor receptor β (PdgfrβF7/F7 mutant mice and their respective controls Pdgfrβ+/+ maintained on a 129S1/SvlmJ background were used. Mice at 2, 4-6, 12-16, and 36-48 weeks of age and of both sexes were used in the study. We also crossed Fibrinogen-deficient (alpha-chain) heterozygous mice (Fga+/-) maintained on a mixed genetic background with F7/F7 mice. Double transgenic F7/F7; Fga+/- mice and their F7/F7; Fga+/+ littermate controls were also used in the study. All procedures were approved by the Institutional Animal Care and Use Committee at the University of Southern California using US National Institutes of Health guidelines. See Online Methods, 'Animals' section.

Policy information about studies involving human research participants

12. Description of human research participants

Describe the covariate-relevant population characteristics of the human research participants.

We used human tissue samples obtained from the Rush University Medical Center and the University of Southern California. Informed consent was obtained and the study approved by the Institutional Review Board of Rush University Medical Center and the University of Southern California. All autopsy cases underwent neuropathological evaluation of AD including assignment of Braak stages. Aged subjects that did not carry diagnosis of AD or another neurodegenerative disease and showed neuropathological findings within the normal range for age were used as age-matched controls. Mini-Mental State Examination information was available for most but not all individuals. A total of 15 controls and 16 AD individuals were used for histopathological analyses. The demographic information of all cases is provided in Supplementary Table 1. See also Online Methods, 'Human Postmortem Studies' section.

Nature Medicine: doi:10.1038/nm.4482

nature research

Corresponding author(s): Berislav V. Zlokovic

Flow Cytometry Reporting Summary

Form fields will expand as needed. Please do not leave fields blank.

Data presentation

For all flow cytometry data, confirm that:

☒ 1. The axis labels state the marker and fluorochrome used (e.g. CD4-FITC).

☒ 2. The axis scales are clearly visible. Include numbers along axes only for bottom left plot of group (a 'group' is an analysis of identical markers).

☒ 3. All plots are contour plots with outliers or pseudocolor plots.

☒ 4. A numerical value for number of cells or percentage (with statistics) is provided.

Methodological details

5. Describe the sample preparation.	Wild type and F7/F7 animals were transcardially perfused with 0.01 M PBS + EDTA and brains immediately removed. White matter tissue (including corpus callosum, internal capsule, cingulum, and external capsule) was isolated from the brains, trypsinized for 30 min in 0.25% trypsin at 37°C and then further dissociated using a glass homogenizer. Cells were fixed in 4% PFA for 10 min, blocked in 10% NDS/0.1% Triton-X/1X PBS, stained with mature oligodendrocyte markers rabbit proteolipid protein (PLP; Abcam, ab105784; 1:2000) and mouse MBP (SMI-99; BioLegend; 1:500), followed by incubation in secondary 488- (Invitrogen; 1:200) and 647-Alexa Fluor (Invitrogen; 1:200) respectively. See Online Methods.
6. Identify the instrument used for data collection.	BD SORP FACSAria I (Becton-Dickinson).
7. Describe the software used to collect and analyze the flow cytometry data.	Data were acquired using FACSDiva 8.0.1 software and analyzed with FlowJo V10.
8. Describe the abundance of the relevant cell populations within post-sort fractions.	Purity was determined by relevant staining using flow cytometry. 10,000 events were originally collected from which positively-gated cells showed 95-98% purity.
9. Describe the gating strategy used.	Control stains (unstained and MBP- or PLP- single stained cells) were used to set gates. All samples were then FSC-A and SSC-A gated, followed by FSC-A/FSC-H gating to select singlet cells. Subsequent relevant gating was conducted. See Online Methods.

Tick this box to confirm that a figure exemplifying the gating strategy is provided in the Supplementary Information. ☒

Nature Medicine: doi:10.1038/nm.4482

Corresponding author(s): Berislav V. Zlokovic

MRI Studies Reporting Summary

Form fields will expand as needed. Please do not leave fields blank.

Experimental design

1. Describe the experimental design.	F7/F7 mice and littermate controls were scanned cross-sectionnaly (at 2, 4-6, 12-16, 36-48 weeks of age) with a Biospec 7T system (300 MHz, Bruker, Billerica, MA, USA) at the California Institute of Technology (Pasadena, CA, USA). The magnet is equipped with the standard B-GA12 gradient set (~12-mm inner diameter; 400 mT.m-1 maximum gradient) and a 35-mm internal diameter quadrature volume coil was used (M2M Imaging, Cleveland, OH). Fibrinogen-deficient and plasminogen-deficient F7/F7 mice and their littermate controls were scanned cross-sectionally (12-16 weeks of age) with our new MR Solutions 7T PET-MR system (MR Solutions Ltd., Guildford, UK) at the Zilkha Neurogenetic Institute (University of Southern California, Los Angeles, CA, USA). The MR Solutions magnet is equipped with the MRS cryogen-free MRI system (bore size ~24-mm, up to 600 mT.m-1 maximum gradient) and a 20-mm internal diameter quadrature bird cage mouse head coil. Comparable sequences and parameters were used with both MR scanners. See Online Methods.
2. Specify the number of blocks, trials or experimental units per session and/or subject, and specify the length of each trial or block (if trials are blocked) and interval between trials.	Total imaging time was approximately 1.5 h per mouse. Mice were scanned cross-sectionnaly at 2, 4-6, 12-16, 36-48 weeks of age.
3. Describe how behavioral performance was measured.	Mice were anesthetized by 1-1.5% isoflurane/air. Respiration rate (80-120 breaths per minute) and body temperature (36.5 ± 0.5°C) are monitored during the experiments using an abdominal pressure-sensitive probe and a rectal temperature probe. The isoflurane dose and heated air flow was adjusted continuously to ensure stable and reproducible depth of anesthesia. ImageJ's Time Series Analyzer V3 plugin was used in real time to ensure good Gd-bolus intravenous injection for both DCE and DSC scans. See Online Methods.

Nature Medicine: doi:10.1038/nm.4482

Acquisition

4. Imaging

a. Specify the type(s) of imaging.	Structural (T2w, T1w, and T2*w), diffusion (DTI-PGSE) and perfusion (DCE and DSC).
b. Specify the field strength (in Tesla).	7T and 11.7T for in vivo and ex vivo scanning sessions, respectively.
c. Provide the essential sequence imaging parameters.	In vivo scans: Pre-contrast T1-values using a variable time repetition (VTR) spin-echo sequence (TR = 5000, 3000, 1500, 800, 400, and 200 ms, RARE factor 3, TE = 11 ms, 1 average, resolution 0.2x0.2x1 mm3), followed by a dynamic series of 800 T1-weighted images with identical geometry and a temporal resolution of 2.6 s (fast low angle shot (FLASH), TR/TE = 20.6/3.2 ms, 2 averages, flip angle 15°, 200x200x1000 µm3). Using a power injector, a bolus dose of 0.5 mmol/kg Gd-DTPA (Gadoliniumdiethylenetriamine pentaacetic acid, Magnevist®, diluted in saline 1:5) is injected via the tail vein (rate of 600 µL/min) at 5 min (volume injected 190 µL) and DCE images are collected for an additional 30 min after the injection. The DSC-MRI imaging is performed on the exact same geometry. A dynamic series of 160 T2*-weighted images is used, with a temporal resolution of 600 ms (FLASH, TR/TE = 18.9/5 ms, 1 average, flip angle 15°, resolution 200x200x1000 µm3). A second bolus dose of Gd-DTPA is injected via the tail vein (rate of 1000 µL/min) at 18 s (volume injected 200 µL) and DSC images are collected for an additional 80 s after the injection. About 1.5 hours scan session per mouse. Ex vivo scans: First, 3D-rapid acquisition with relaxation enhancement (RARE) anatomical images were acquired (TR/TE = 250/9 ms; RARE factor 8; 140x80x80 matrix; 28x16x16 mm FOV, 200 µm isotropic voxel size; 1 average). Then, DWIs were acquired using a conventional pulsed-gradient spin echo (PGSE) sequence (TR/TE = 300/16.2 ms, 350×200x200 matrix, 28x16x16 mm FOV, 80 µm isotropic voxel size, 1 average, δ = 3 ms, Δ = 8 ms, Gd = 1000 mT/m, nominal b-factor = 3000 s/mm2). Six diffusion weighted images were acquired in addition to one volume with no diffusion sensitization using an optimized six points icosahedral encoding scheme for a total imaging time of 24 h. Plus, an additional high-resolution T2*-weighted was acquired using a FLASH sequence (TR/TE = 50/5.19 ms, 400x200x240 matrix, 28x16x16 mm FOV, 50 µm isotropic voxel size, averages 18) for a total imaging scan of 12 h. See Online Methods.
d. For diffusion MRI, provide full details of imaging parameters.	DWIs were acquired ex vivo using a conventional pulsed-gradient spin echo (PGSE) sequence (TR/TE = 300/16.2 ms, 350×200x200 matrix, 28x16x16 mm FOV, 80 µm isotropic voxel size, 1 average, δ = 3 ms, Δ = 8 ms, Gd = 1000 mT/m, nominal b-factor = 3000 s/mm2). Six diffusion weighted images were acquired in addition to one volume with no diffusion sensitization using an optimized six points icosahedral encoding scheme for a total imaging time of 24 h.
5. State area of acquisition.	DCE and DSC where 2 slices (thickness 1-mm) were selected within the dorsal hippocampus territory and the prefrontal cortex to guarantee having WM areas such as corpus callosum, internal and external capsule, and cingulum, as well as common carotid arteries for arterial input functions. See Onlline Methods.

Nature Medicine: doi:10.1038/nm.4482

Preprocessing

6. Describe the software used for preprocessing.

To pre-process the raw ex vivo DWIs, we first corrected for eddy current distortions using the “eddy correct” tool in FSL (www.fmrib.ox.ac.uk/fsl). Extra cerebral tissue was removed using the “skull-stripping” Brain Extraction Tool from BrainSuite (http://brainsuite.org/). All resulting volumes were visually inspected and manually edited as needed. Then, all images were linearly aligned using FSL’s “flirt” function with 12 degrees of freedom to allow for rotation, translation, scaling, and skewing in 3D. The gradient direction tables were rotated accordingly after each linear registration for the 6 diffusion volumes. Furthermore, each skull-stripped b0 images were elastically registered to a minimum deformation template created using all linearly registered images for both +/+ and F7/F7 mice. This was done to ensure that all scans were in the same space for further analysis.

To process in vivo T1-VTR and DCE scans, we used our in-house T1 mapping/DCE processing software (Rocketship) implemented in Matlab (Barnes, S. R. et al. ROCKETSHIP: a flexible and modular software tool for the planning, processing and analysis of dynamic MRI studies. BMC Med. Imaging 15, 19 (2015)). Available here: https://github.com/petmri/ROCKETSHIP. To process DSC perfusion data, we used another in-house Matlab script.

7. Normalization

a. If data were normalized/standardized, describe the approach(es).

N/A

b. Describe the template used for normalization/transformation.

N/A

8. Describe your procedure for artifact and structured noise removal.

Linear alignement (for DWI) and motion correction (for DCE/DSC) were applied using FSL's "flirt" function and ImageJ's Stack Reg - Rigid Body plugin, respectively.

9. Define your software and/or method and criteria for volume censoring, and state the extent of such censoring.

N/A

Statistical modeling & inference

10. Define your model type and settings.

N/A

11. Specify the precise effect tested.

We measured BBB permeability and CBF dysfunction using DCE and DSC techniques, respectively; WM integrity and volumetric changes using 3D DWI datasets; and hemosiderin deposits using 3D T2*-weighted sequence.

12. Analysis

a. Specify whether analysis is whole brain or ROI-based.

The analysis is ROI-based except for DTI-tractography mapping where the whole brain was used.

b. If ROI-based, describe how anatomical locations were determined.

The brain regions-of-interest boundaries were manually drawn for each slice using ImageJ and a mouse brain anatomical atlas (Allen Mouse Brain Atlas).

13. State the statistic type for inference. (See Eklund et al. 2016.)

To test for group differences, a voxel-wise linear regression was run, with F7/F7 mice coded as 1 and +/+ mice coded as 0. See Online Methods for more details, as well as 1/ Daianu, M. et al. 7T Multi-shell Hybrid Diffusion Imaging (HYDI) for Mapping Brain Connectivity in Mice. Proc. SPIE-- Int. Soc. Opt. Eng. 9413, (2015) and 2/ Daianu, M., Jacobs, R. E., Weitz, T. M., Town, T. C. & Thompson, P. M. Multi-Shell Hybrid Diffusion Imaging (HYDI) at 7 Tesla in TgF344-AD Transgenic Alzheimer Rats. PloS One 10, e0145205 (2015).

Nature Medicine: doi:10.1038/nm.4482

14. Describe the type of correction and how it is obtained for multiple comparisons.	For DTI metrics and tractography mapping, a regional false discovery rate (FDR) correction was used to correct for multiple comparisons across voxels. Additionally, searchlight-based multivoxel pattern statistics were performed on the resulting probabilistic p-value maps from the regression in all cohorts.
15. Connectivity	
a. For functional and/or effective connectivity, report the measures of dependence used and the model details.	N/A
b. For graph analysis, report the dependent variable and functional connectivity measure.	N/A
16. For multivariate modeling and predictive analysis, specify independent variables, features extraction and dimension reduction, model, training and evaluation metrics.	N/A

Nature Medicine: doi:10.1038/nm.4482